Solar Phys (2017) 292:127
DOI 10.1007/s11207-017-1148-6

Origin of Radio Enhancements in Type II Bursts in the Outer Corona

Firas Al-Hamadani[1,2] · Silja Pohjolainen[1,3] · Eino Valtonen[1]

Received: 29 November 2016 / Accepted: 21 July 2017 / Published online: 31 August 2017
© Springer Science+Business Media B.V. 2017

Abstract We study interplanetary (IP) solar radio type II bursts from 2011 – 2014 in order to determine the cause of the intense enhancements in their radio emission. Type II bursts are known to be due to propagating shocks that are often associated with fast halo-type coronal mass ejections (CMEs). We analysed the radio spectral data and the white-light coronagraph data from 16 selected events to obtain directions and heights for the propagating CMEs and the type II bursts. CMEs preceding the selected events were included in the analysis to verify whether CME interaction was possible. As a result, we were able to classify the events into five different groups. 1) Events where the heights of the CMEs and type II bursts are consistent, indicating that the shock is located at the leading front of the CME. The radio enhancements are superposed on the type II lanes, and they are probably formed when the shock meets remnant material from earlier CMEs, but the shock continues to propagate at the same speed. 2) Events where the type II heights agree with the CME leading front and an earlier CME is located at a height that suggests interaction. The radio enhancements and frequency jumps could be due to the merging process of the CMEs. 3) Events where the type II heights are significantly lower than the CME heights almost from the start. Interaction with close-by streamers is probably the cause for the enhanced radio emission, which is located at the CME flank region. 4) Events where the radio enhancements are located within wideband type II bursts and the causes for the radio enhancements are not clear. 5) Events where the radio enhancements are associated with later-accelerated particles (electron beams, observed as type III bursts) that stop at the type II burst emission lane, and no other obvious reason for the enhancement can be identified.

✉ F. Al-Hamadani
fimubaa@utu.fi

S. Pohjolainen
silpoh@utu.fi

E. Valtonen
eino.valtonen@utu.fi

1 Department of Physics and Astronomy, University of Turku, Turku, Finland

2 Department of Physics, University of Basrah, Basrah, Iraq

3 Tuorla Observatory, University of Turku, Piikkiö, Finland

Most of the events (38%) were due to shock–streamer interaction, while one quarter of the events was due to possible CME–CME interaction. The drift rates, bandwidth characteristics, or cross-correlations of various characteristics did not reveal any clear association with particular category types. The chosen atmospheric density model causes the largest uncertainties in the derived radio heights, although in some cases, the emission bandwidths also lead to relatively large error margins.

Our conclusion is that the enhanced radio emission associated with CMEs and propagating shocks can have different origins, depending on their overall configuration and the associated processes.

Keywords Coronal mass ejections · Initiation and propagation · Radio bursts · Meter-wavelengths and longer (m, dkm, hm, km) · Type II

1. Introduction

The large-scale expulsions of plasma and magnetic fields from the Sun into the interplanetary (IP) medium are known as coronal mass ejections (CMEs). The particles accelerated in the solar corona and in the IP medium can be observed at radio wavelengths as they propagate through space. Solar radio type II bursts are known to be due to coronal and/or CME-driven shocks because the shocks accelerate electrons and the plasma oscillations turn into radio waves (*e.g.* Cairns *et al.*, 2003). Previous studies confirm that type II bursts at decametric–hectometric (DH) and longer wavelengths are caused by shocks driven by CMEs in the IP space (Cane, Sheeley, and Howard, 1987; Bale *et al.*, 1999; Gopalswamy *et al.*, 2001a).

Suprathermal electrons that are generated in solar flares and injected into the IP medium produce radio type III bursts (Lin *et al.*, 1981). Continuous type III bursts can also appear as radio storms (Kai, Melrose, and Suzuki, 1985). Complex long-duration type III radio bursts associated with large flares are typically also associated with CMEs (Reiner *et al.*, 2000).

It has been discovered that interacting CMEs can produce radio enhancements (Gopalswamy *et al.*, 2001b, 2002). A shock wave driven by a fast CME can catch up with an earlier slower CME, causing the shock to strengthen or weaken. Vandas *et al.* (1997) suggested that the shock was weakening when it passed through a preceding CME especially near 1 AU, but Wu, Wang, and Gopalswamy (2002) and Odstrcil *et al.* (2003) claimed the opposite. Gopalswamy *et al.* (2001a), Burlaga, Plunkett, and St. Cyr (2002), and Temmer *et al.* (2012) have suggested that CMEs may merge and then propagate as a single magnetic structure. Martínez Oliveros *et al.* (2012) used a direction-finding technique to locate the observed radio emission of the 1 August 2010 type II burst and suggested that the CME interaction produced the observed enhanced type II emission. The same event was studied by Temmer *et al.* (2012), and they concluded that the interaction between magnetic structures of the CMEs started early, before the leading edges of the CMEs were merged.

In this article we study CME events that showed enhanced radio emission on top of typical type II burst emission. The event selection was based on the radio enhancement signatures that were identified in the radio dynamic spectra at DH wavelengths. We then compared the radio data to CME imaging data to determine possible causes for the enhanced emission.

2. Data Analysis

We searched for IP radio type II bursts with signatures of enhanced emission using radio observations from 2011 – 2014. This time period gives a good data coverage for SOHO (*Solar and Heliospheric Observatory*), *Wind*, and STEREO (*Solar Terrestrial Relations Observatory*) observations, with the STEREO twin satellites on the opposite sides of the Sun. In the selection of events, we required that an identifiable propagating CME must be present, associated with a radio type II burst. We then searched for any preceding CMEs that originated from the same or nearby active regions, with the idea that they could have affected the propagation of the later CME or the type II shock, and could have been involved in the formation of the radio enhancement signatures.

With these criteria, we found a total of 16 events. The characteristics of the primary CMEs (hereafter CME2), earlier CMEs (hereafter CME1), and their associated flares are listed in Table 1.

The data for the IP radio type II events were taken from the *Wind*/WAVES (*Plasma and Radio Waves*; Bougeret *et al.*, 1995) catalogue, prepared by Michael L. Kaiser. The STEREO/WAVES (SWAVES) (Bougeret *et al.*, 2008) dynamic spectra were obtained from the NASA GSFC online catalogue. The CDAW LASCO CME Catalog was used to look up the CME characteristics as observed by SOHO/*Large Angle and Spectrometric Coronagraph* LASCO (Brueckner *et al.*, 1995) and STEREO/*Sun Earth Connection Coronal and Heliospheric Investigation* SECCHI (Howard *et al.*, 2008). The flare data are from SWPC (Space Weather Prediction Center) and NOAA/NCEI (National Centers for Environmental Information). The flare locations were also verified from EUV images provided by SOHO/*Extreme ultraviolet Imaging Telescope* EIT (Delaboudinière *et al.*, 2014) and the STEREO/SECCHI/EUVI telescopes (Wuelser *et al.*, 2004). Solar X-ray fluxes were measured by GOES (*Geostationary Operational Environmental Satellite*).

2.1. Comparison of Radio Emission and CME Heights

The observed radio frequency [f] in Hz depends on the local electron density [n_e], in cm^{-3}, by $f = 9000\sqrt{n_e}$. The methods for determining type II burst heights using atmospheric density models have been described in *e.g.* Pohjolainen *et al.* (2007). This article also quantifies the different height values obtained in the frequency range of 500 MHz – 1 MHz when using different atmospheric density models. The atmospheric electron density model by Vršnak, Magdalenič, and Zlobec (2004), called the hybrid density model, is a model that merges the high-density low-corona models with the low-density IP models without breaks or discrepancies. The hybrid density model is basically a mixture of the five-fold model of Saito (1970) and the Leblanc, Dulk, and Bougeret (1998) model, with small modifications.

We used the hybrid density model to calculate the radio source heights for all our events. As most of the radio enhancements in our study occurred below the frequency of 1 MHz, we estimated how selecting an atmospheric density model would affect the height estimates at low frequencies. At 1 MHz the plasma density is 1.23×10^4 cm^{-3}, which can be determined to be low enough not to represent high-density active region loops, and therefore we can exclude high-density low-corona models like the ten-fold model of Saito and the two-fold model of Newkirk (1961). At 1 MHz, the hybrid model gives a height of 10.36 R$_\odot$ and the basic one-fold model of Saito a height of 8.58 R$_\odot$, which gives a difference of 1.78 R$_\odot$. As the frequency decreases, the height difference between the models also decreases. At 500 kHz, the height difference is 0.95 R$_\odot$, and at 200 kHz (the lowest start frequency in our sample), the difference is only 0.14 R$_\odot$. Our error estimates based on the model selection

Table 1 Characteristics of the preceding CMEs (CME1, in italics), the primary CMEs (CME2), and their associated flares. CME time is the time of first observation, and CME speed is from a linear fit to the CME leading front observations (LASCO CME Catalog).

Event	Date dd/mm/yyyy	CME time (UT)	CME speed ($km\,s^{-1}$)	Flare class (GOES)	Flare location	Active Region (NOAA)
1	*14/02/2011*	*18:24*^{H}	*326*	*M2.2*	*S20W04*[1]	*11158*
	15/02/2011	02:24^{H}	669	X2.2	S20W12[1]	11158
2	*07/03/2011*	*14:48*^{P}	*698*	*M1.9*	*N10E18*	*11166*
	07/03/2011	20:00^{H}	2125	M3.7	N30W48	11164
3	*21/09/2011*	*10:12*	*229*	–	N15E100	–
	22/09/2011	10:48^{H}	1905	X1.4	N09E89	11302
4	*26/11/2011*	*00:36*	*292*	–	–	–
	26/11/2011	07:12^{H}	933	C1.5	N11W47	11357^{F}
5	*19/01/2012*	*09:48*	*317*	–	–	–
	19/01/2012	14:36^{H}	1120	M3.2	N32E22	11402
6	23/01/2012	03:12^{P}	684	M8.7	N28W21	11402
	23/01/2012	04:00^{H}	2175	M8.7	N28W21	11402
7	*05/03/2012*	*03:12*	*594*	*X1.1*	*N16E54*	*11429*
	05/03/2012	04:00^{H}	1531	X1.1	N16E54	11429
8	*10/03/2012*	*16:24*^{P}	*423*	*C8.0*	*N15W36*	*11430*
	10/03/2012	18:00^{H}	1296	M8.4	N17W24	11429
9	*16/05/2012*	*15:36*	*306*	–	–	–
	17/05/2012	01:48^{H}	1582	M5.1	N11W76	11476
10	*17/07/2012*	*13:25*	*292*	–	–	–
	17/07/2012	13:48^{P}	958	M1.7	S28W65	11520
11	*31/08/2012*	*11:12*	*706*	*C1.3*^{U}	*S21E63*	*11563*
	31/08/2012	20:00^{H}	1442	C8.4	S19E42	11562^{F}
12	*12/03/2013*	*23:48*	*481*	*C1.8*	*N06E41*	*11692*
	15/03/2013	07:12^{H}	1063	M1.1	N11E12	11692
13	*22/05/2013*	*08:48*^{P}	*687*	*C2.3*	*N17W62*	*11745*
	22/05/2013	13:25^{H}	1466	M5.0	N15W70	11745
14	*29/09/2013*	*01:48*	*374*	–	–	–
	29/09/2013	22:12^{H}	1179	C1.2	N10W33	11850^{F}
15	*07/01/2014*	*03:36*^{P}	*688*	–	S15W125	–
	07/01/2014	18:24^{H}	1830	X1.2	S15W11	11943/11944
16	*18/04/2014*	*07:24*	*387*	*C1.6*	*S16W31*	*12036*
	18/04/2014	13:25^{H}	1203	M7.3	S20W34	12036

[1] Shanmugaraju *et al.* (2014).

^{H} Halo CME.

^{P} Partial-halo CME.

^{F} Filament eruption (large scale).

^{U} Uncertain association.

are therefore ~ 2 $R_\odot$ near 2 – 1 MHz, ~ 1 $R_\odot$ near 500 kHz, and 0.1 – 0.3 $R_\odot$ near 200 – 150 kHz (150 kHz being the lowest frequency where we traced the radio emission; near this frequency the height difference also increases slightly).

For the type II burst lanes and also for the enhanced emission 'patches', the lane centre was taken as the frequency from which the heights were calculated. In events that show wide-band emission, this causes large uncertainty in the height estimates, while in narrow-band events, the uncertainty is much smaller. As lanes and lane centres are determined by eye from the dynamic spectrum, the human factor may also cause some error in the height estimates. Last, as plasma processes may vary and the emission may be produced at different parts of the shock front (*e.g.*, band-split to up-stream and down-stream regions), definite error bars to the determined radio source heights cannot be given.

Uncertainties in the CME heights are produced by projection effects. The listed CME heights in Table 2 are the observed (projected) leading front heights from SOHO/LASCO observations. These may not be the real leading fronts, especially if the CME is propagating toward the observer. To overcome this problem, we also analysed the coronagraph images from STEREO A and STEREO B to verify the heights of the CME leading fronts, and we also compared our results with those obtained in earlier studies, when available.

Table 2 lists the calculated radio emission heights at the start time of the radio enhancement. The observed and estimated CME1 and CME2 heights from SOHO/LASCO observations are also given, with the height difference of the CMEs at the time of the radio enhancement start. The CME heights contain both observed and interpolated heights, and extrapolated heights are marked in italics. For the CME height estimation, we used both linear and second-order fits.

2.2. 3D View of the Events

We summarise here the observations of each of the 16 events. To estimate the 3D properties and gain a better understanding of the type II burst propagation, we investigated *Wind*/WAVES (hereafter WAVES), STEREO A/SWAVES (hereafter SWAVES A), and STEREO B/SWAVES (hereafter SWAVES B) observations of the type II radio bursts, available at http://swaves.gsfc.nasa.gov/data_access.html. The comparison of the radio type II burst heights observed with the instruments in the three different spacecraft are shown for each event in Figures 1 – 16.

In each of the event figures, a schematic drawing explains the locations of the CMEs observed from Earth, and nearby streamers are also marked in the drawings. A SOHO/LASCO coronagraph difference image is shown near the time of the radio enhancement start, with the corresponding WAVES dynamic spectrum. Height–time plots show the time evolution of the CME leading fronts and the radio features. In the plots the radio enhancements are marked with a purple line that connects the heights at the start and near the end of the enhanced emission, but we note that the propagation of these structures may not be linear. Type II burst heights are given at selected time intervals, and colours indicate the different instruments (WAVES in green, SWAVES A in red, SWAVES B in blue). The CME heights observed by SOHO/LASCO (Earth view) are from the LASCO CME Catalog. The plane-of-sky CME heights observed by STEREO/SECCHI (viewed from STEREO A or STEREO B locations) were measured by us. The direction (position angle, PA, measured counter-clockwise from solar north, in degrees) was selected so that it matches the CME leading front direction observed by LASCO. For example, when the CME propagated in the western side of the Sun as observed by LASCO, we measured the leading front heights using STEREO A observations. When the leading front of the CME was not clear from this direction, we used the other STEREO view.

Table 2 Observed and estimated (in italics) heights for CME1 and CME2, and their height difference, ΔH, and radio source heights and frequencies at the time of the radio enhancement start. The method of calculating radio emission heights is explained in the text.

No.	Date	Time UT	Radio freq. kHz	Radio height $R_\odot$	CME1 H1 $R_\odot$	CME2 H2 $R_\odot$	ΔH H1 – H2 $R_\odot$
1	15 Feb. 2011	04:48	700	12.6	*19.5*	11.0	8.5
2	08 Mar. 2011	00:06	225	27.2	*37.0*	*49.0*	−12.0
3	22 Sep. 2011	16:19	400	18.0	*39.5*	*66.0*	−26.5
4	26 Nov. 2011	09:18	1000	10.2	15.5	13.0	1.5
		15:42	200	30.0	*31.5*	*44.0*	−12.5
5	19 Jan. 2012	18:41	500	15.5	*16.5*	*25.0*	−8.5
6	23 Jan. 2012	08:20	350	18.19	–	*55.0*	–
		12:25	250	22.0	–	$\gg$ *55.0*	–
7	05 Mar. 2012	06:30	700	12.6	*13.0*	24.5	−11.5
		07:36	400	18.0	*17.0*	*35.0*	−18.0
8	10 Mar. 2012	18:42	2200	6.7	8.0	7.5	0.5
		20:18	320	21.0	*11.5*	19.0	−7.5
9	17 May 2012	03:30	950	10.5	21.5	17.8	3.7
10	17 Jul. 2012	19:06	400	18.0	11.7	*29.0*	−17.3
11	31 Aug. 2012	22:06	900	10.9	*42.0*	19.0	23.0
		23:33	500	15.5	$>$ *50.0*	29.5	$>$ 20.0
12	15 Mar. 2013	15:00	250	25.1	–	*47.0*	–
13	22 May 2013	14:42	1000	10.2	22.5	15.0	7.5
14	29 Sep. 2013	23:06	1500	8.2	*45.0*	8.5	36.5
		00:12	660	13.1	*47.0*	15.5	31.5
15	07 Jan. 2014	20:06	400	18.0	$>$ *50.0*	21.5	$>$ 28.0
16	18 Apr. 2014	14:42	1000	10.2	*17.0*	12.5	4.5
		15:51	700	12.6	*19.0*	19.0	0.0
		17:07	500	15.5	*22.0*	*29.0*	−7.0

2.2.1. Radio Event 1: 15 February 2011

The primary halo CME2 (Figure 1) originated from the south-western hemisphere and was associated with an X2.2 class X-ray flare. The linear fit from the LASCO observations gives a speed of 669 km s^{-1}, but a lower initial speed of 557 km s^{-1} was obtained from the 3D 'croissant' modelling by Möstl *et al.* (2014). The radial speeds from flux-rope and cone-model fits by Xie *et al.* (2013) produced speeds of 651 and 624 km s^{-1}, respectively, which shows that the speeds obtained with different methods are quite similar.

The preceding CME1 originated from the same active region the day before, about eight hours earlier, and it was associated with an M2.2 class flare. The flare locations have been determined by Shanmugaraju *et al.* (2014). This CME was slow, with a linear fit speed of 326 km s^{-1}. Maričić *et al.* (2014) have derived significantly larger heights for CME1 compared to our constant-speed extrapolation shown in Figure 1. However, their heights of CME2 in the early phase (below 15 $R_\odot$) agree reasonably well with our measurements from STEREO A.

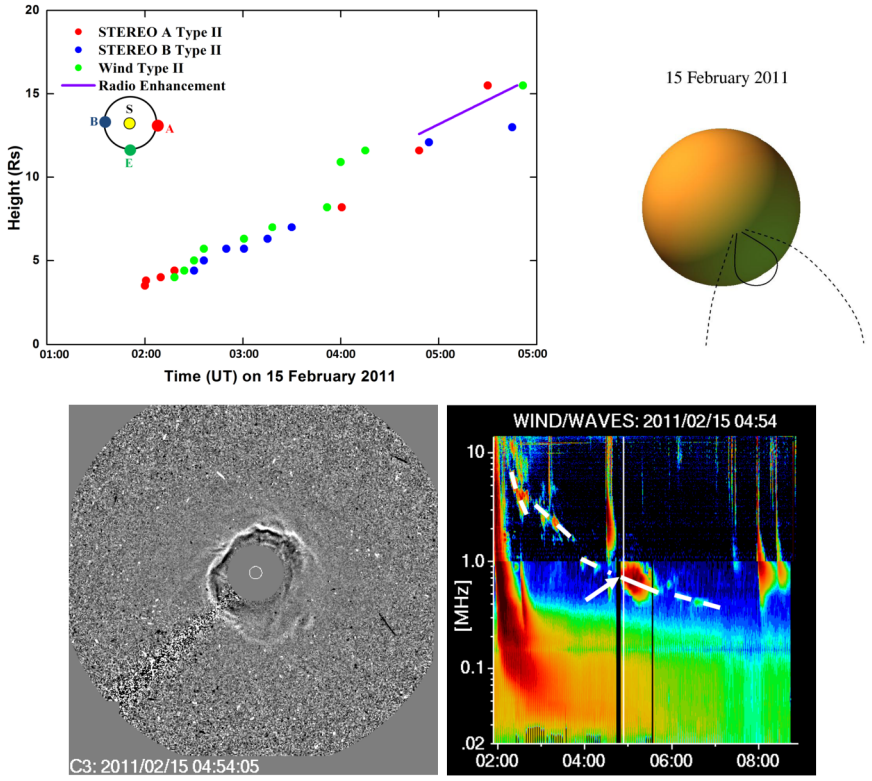

Figure 1 Observed and calculated data for the event on 15 February 2011. The *upper right panel* is a schematic drawing showing the locations and directions of CME1 (*dashed line*) and CME2 (*solid line*) near the time when CME2 was launched (drawing not to scale). Streamers are drawn in *brown*, but only those are shown that were located nearby the CMEs, if any. The *upper left panel* shows the calculated heights of the radio type II bursts observed by the instruments onboard three different spacecraft, STEREO A, STEREO B, and *Wind*. Also the spacecraft positions around the Sun are schematically shown in the plot. The *middle right panel* shows the *Wind*/WAVES radio dynamic spectrum near the time of the radio enhancement. *Dashed white lines* trace the type II burst lanes, and the *solid white line* indicates the radio enhancement. *White arrow* points to the start time of the radio enhancement. The *middle left panel* shows the SOHO/LASCO C3 image near the start time of the radio enhancement. The *bottom panel* (next page) shows the height–time plot of the CMEs observed by SOHO/LASCO and STEREO/SECCHI and the linear fits or extrapolations to linear fits of LASCO data. The calculated radio type II burst heights (from *Wind*) and the estimated radio enhancement heights are also shown. The LASCO image and the WAVES spectral plot are from the LASCO CME Catalog.

The radio type II burst associated with CME2 was first identified at metric wavelengths, and the burst continued to DH wavelengths, showing emission patches along identifiable lanes. At the start, emission at the fundamental and harmonic frequencies was visible. SWAVES A, WAVES, and SWAVES B all observed the radio bursts, so the emission source was visible from all three directions. At 7 – 3 MHz, the type II burst was observed at about the time of the CME2 launch seen by LASCO, which was about one hour after the CME2 launch was observed by STEREO. Based on the hybrid density model, the shock speed was 1100 km s^{-1}, and at the time of the 7 – 3 MHz emission, the shock could not yet have reached CME1. This was also the conclusion of Temmer *et al.* (2014), and in spite of the intermittency of the radio emission, we consider this as usual type II emission.

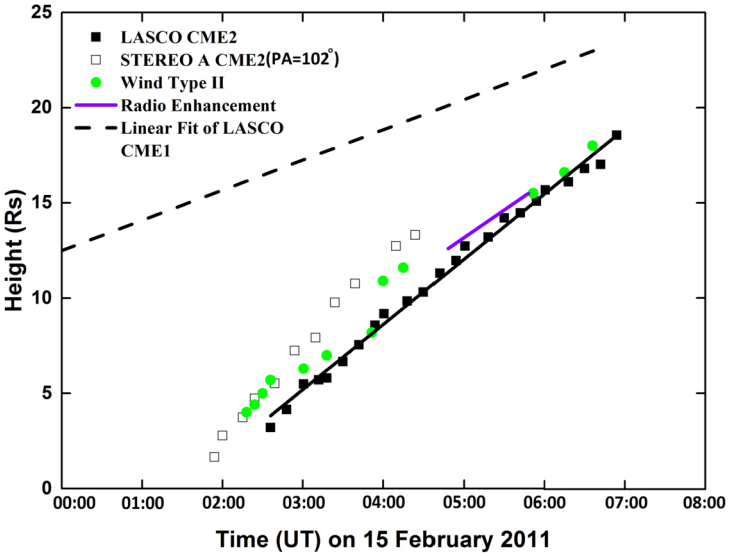

Figure 1 (*Continued*)

The radio enhancement was observed two hours later as an extended wide-band structure along the fundamental emission lane of the type II burst. The height separation of the leading fronts of the two CMEs was estimated at that time to be about 8.5 $R_{\odot}$ (SOHO view). However, the CME2 heights determined from STEREO A observations are several solar radii higher, and therefore the height difference to CME1 could have been smaller, suggesting that the radio emission started when the front of CME2 reached the rear parts of CME1. From the viewing point of STEREO A the projection effects were minimal, so that these measurements can be considered more accurate, while measurements from LASCO observations obviously suffer from projection effects.

Maričić *et al.* (2014) suggested that CME1 – CME2 interaction took place at a height of $\sim 28-45$ $R_{\odot}$ at $\sim 8-13$ UT, about two hours after the end of the radio enhancement. CME interaction was suggested by Shanmugaraju *et al.* (2014), based on the appearance of the radio enhancement. They estimated that the CME interaction occurred around 05:00 – 10:00 UT in the height range of $20-25$ $R_{\odot}$, and the shock height for the radio enhancement region was $10-30$ $R_{\odot}$.

Our result is in agreement with Shanmugaraju *et al.* (2014) about the start times and the corresponding heights of the interaction, but we note that the main radio signature of the CME interaction had a shorter duration (about one hour). We have also observed that there was a strong type III burst emission just before the radio enhancement start, possibly bringing more accelerated particles to the emission region.

2.2.2. Radio Event 2: 7 March 2011

The halo CME2 (Figure 2) originated from the north-western hemisphere, and it was associated with an M3.7 class flare. The linear fit from the LASCO observations gives a CME speed of 2125 km s^{-1}, which is similar to the speed obtained by Xie *et al.* (2013) using a flux-rope model fit, 2283 km s^{-1}.

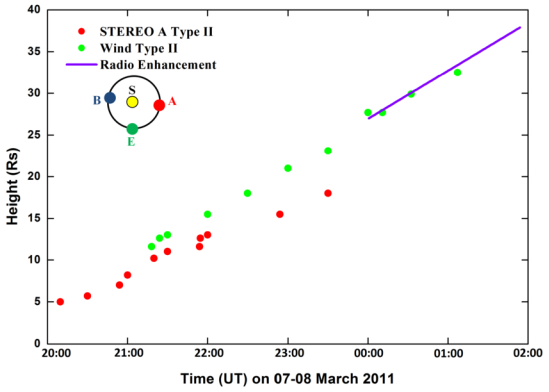

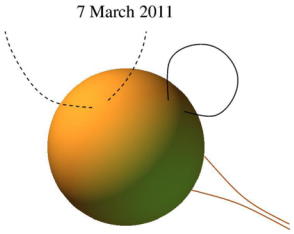

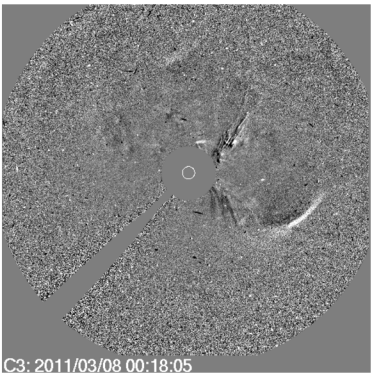

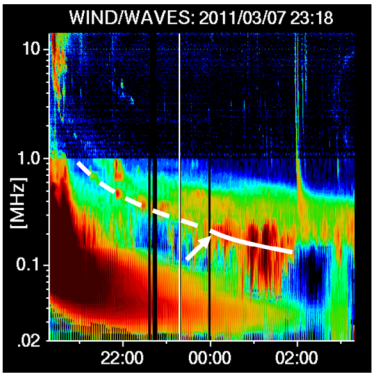

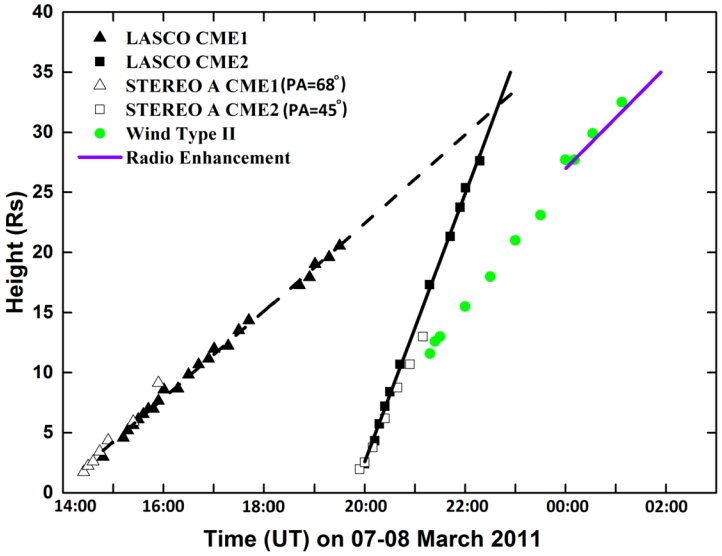

Figure 2 Observed and calculated data for the event on 7 March 2011. *Panels* and *symbols* are the same as in Figure 1.

The earlier CME1 originated from a different active region located in the north-eastern hemisphere, and it was associated with an M1.9 class flare. This CME had a linear fit speed of 698 km s^{-1}, but Xie *et al.* (2013) obtained a higher speed of 863 km s^{-1} using the flux-rope model.

Both CMEs were associated with a type II radio burst. The fundamental emission lane associated with CME1 did not continue below 7 MHz, and so the shock propagation could not be followed after 14:40 UT. The CME2 associated type II burst was well observed by WAVES, but SWAVES A observed only a faint type II at start and then a separate smooth wide-band emission lane. SWAVES B did not observe type II emission, which suggests that the type II burst source was located on the west side of the Sun. As the type II burst heights are significantly lower than the CME2 heights, the burst source could have been located in the western flanks of the CME2.

The first small radio enhancement appeared in the spectrum at ∼22:00 UT at 5 MHz (height ∼4.5 R$_\odot$), but the main strong radio enhancement appeared quite late, at an estimated height of ∼27 R$_\odot$, near 00:06 UT on 8 March. Xie *et al.* (2013) compared the type II shock time–distance profiles with those obtained with the ENLIL model, and suggested this to be an interaction event, with a merging of the two CMEs near 23:10 UT. However, we suggest that the radio enhancement could have been located on the south-western side of the Sun (away from the interaction region of the two CMEs), and that CME2 flank–streamer interaction could have been the cause of the enhanced radio emission. In the LASCO C3 image at 00:18 UT there is a clear (bright) front visible at about the height of the type II burst, in the south-west.

2.2.3. Radio Event 3: 22 September 2011

The halo CME2 (Figure 3) originated from the north-eastern limb and was associated with an X1.4 class flare. The linear fit from the LASCO observations gives a CME speed of 1905 km s^{-1}.

The earlier CME1 originated most probably from the same active region. At the time of CME1 launch, this active region was at longitude ∼E100. STEREO B EUVI showed continuous activity in this region, but we could not identify a specific flare associated with CME1. This CME was very slow, with a linear fit speed of 229 km s^{-1}. The time difference between the two CMEs was 24 hours, making it highly improbable that they interacted by merging.

The type II burst associated with CME2 was first observed at metric wavelengths, where it showed both fundamental and harmonic emission (Zucca *et al.*, 2014). Based on the analysis that used 2D density maps of the low corona, Zucca *et al.* (2014) found that the observations were consistent with the formation of a shock located at the CME flanks, where the Alfvén speed has a local minimum.

Our type II burst height measurements in the IP space confirm that the type II burst source was located in a lower region than the CME leading front. This suggests that the shock continued to propagate at the CME flanks. As WAVES and SWAVES B observed almost similar-looking type II emission and SWAVES A almost nothing, the propagation direction of the shock was towards the STEREO B spacecraft and with a good view toward the Earth. A few type III bursts were also observed to stop at the frequency of the type II burst emission lane.

If CME1 and CME2 continued to propagate with the speeds they were last observed to have, the CME fronts would have had the same height near 37 R$_\odot$. The enhanced radio emission was observed to start about two hours later, with an estimated height of 18 R$_\odot$. We

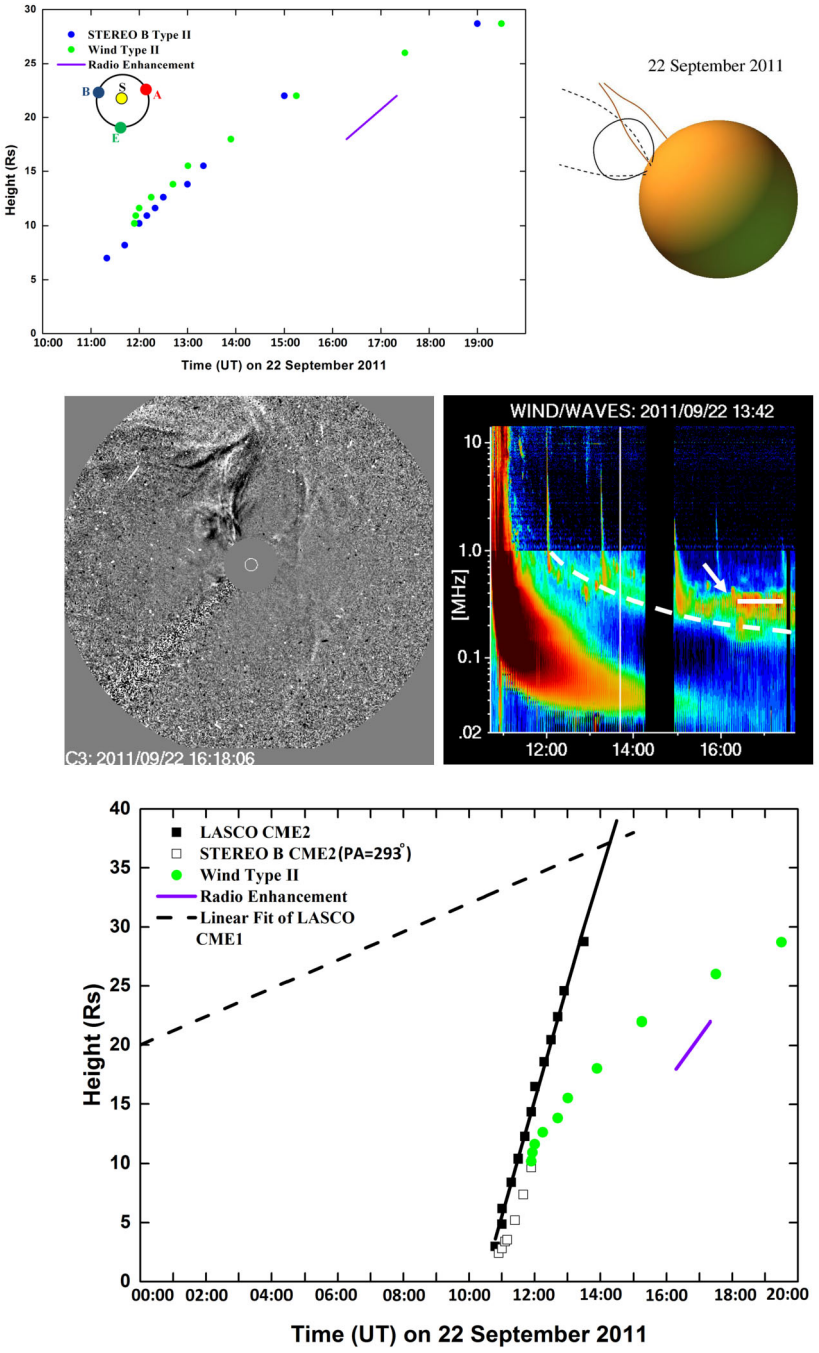

Figure 3 Observed and calculated data for the event on 22 September 2011. *Panels* and *symbols* are the same as in Figure 1.

suggest that CME2 flank interaction with the nearby streamer on the north-eastern side of the Sun is the most probable source for the radio enhancement.

2.2.4. Radio Event 4: 26 November 2011

The halo CME2 originated from the western hemisphere (Figure 4) and was associated with a C-class flare and a filament eruption. The CME2 had a linear fit speed of 933 km s^{-1}. The earlier CME1 propagating to the same direction had a speed of 292 km s^{-1}, but no associated flare could be identified.

The CME2 was associated with an IP type II burst, and Gopalswamy *et al.* (2015) estimated that the shock was formed at a height of 3.25 R$_{\odot}$. According to their analysis, the peak speed of CME2, 1187 km s^{-1}, was not achieved until after the shock formation heights. The IP type II burst showed sporadic emission at the start, with narrow-band lanes. Both WAVES and SWAVES A observed this emission, while SWAVES B saw only one very faint type II burst lane. The first radio enhancement was observed by WAVES and SWAVES A, but only WAVES observed the enhanced emission after 15:40 UT.

The start time of the first radio enhancement coincides with the time when the leading fronts of the two CMEs reached the same height, suggesting that the enhanced emission was due to interaction and merging of the two CMEs.

The later radio enhancement was observed only by WAVES, after the merging process of the CMEs should have been completed. If the emission source was located in the south-west, near the streamer, the view of SWAVES B would have had been obstructed because of geometry, and the view of SWAVES A would have been blocked by the merged CME itself. The height–time plot suggests that CME–streamer interaction could have been possible and so this enhancement would have had a different source origin compared to the first enhancement.

2.2.5. Radio Event 5: 19 January 2012

The halo CME2 (Figure 5) originated from the north-eastern hemisphere and was associated with an M3.2 class flare. The linear fit from the LASCO observations gives a speed of 1120 km s^{-1}, but a much higher speed, 1335 km s^{-1}, was obtained from the 3D modelling by Möstl *et al.* (2014). Liu *et al.* (2013) studied this CME in detail using the coronagraph data from STEREO. They reported impulsive acceleration up to about 15 R$_{\odot}$ (until about 18:40 UT), after which a rapid deceleration took place out to about 35 R$_{\odot}$, and then the CME had a roughly constant speed of about 700 – 800 km s^{-1} (see their Figure 3).

The earlier CME1 that could have affected the propagation of CME2 had a low speed of 317 km s^{-1} and an unidentified origin near the north polar region. As is shown in Figure 5, the leading fronts of CME1 and CME2 reached the same height of 13 R$_{\odot}$ at 16:50 UT, but contact at the CME flanks could have been possible. The rapid deceleration of CME2 above the height of 15 R$_{\odot}$ could be a sign of the two CMEs merging. The roughly constant speed after 35 R$_{\odot}$ would then indicate that the merging had ended and the two CMEs had become one.

Several separate type II burst lanes were observed during the CME2 propagation. These lanes were mostly visible in the WAVES spectrum, and only faint emission features were observed by SWAVES A and B. Liu *et al.* (2013) interpreted the type II burst as a one-lane event, but Teklu *et al.* (2016) identified at least four separate type II lane components. Our analysis shows that the first three type II burst parts had both fundamental and harmonic emission lanes, but the two lanes visible during the fourth burst part (which showed the radio

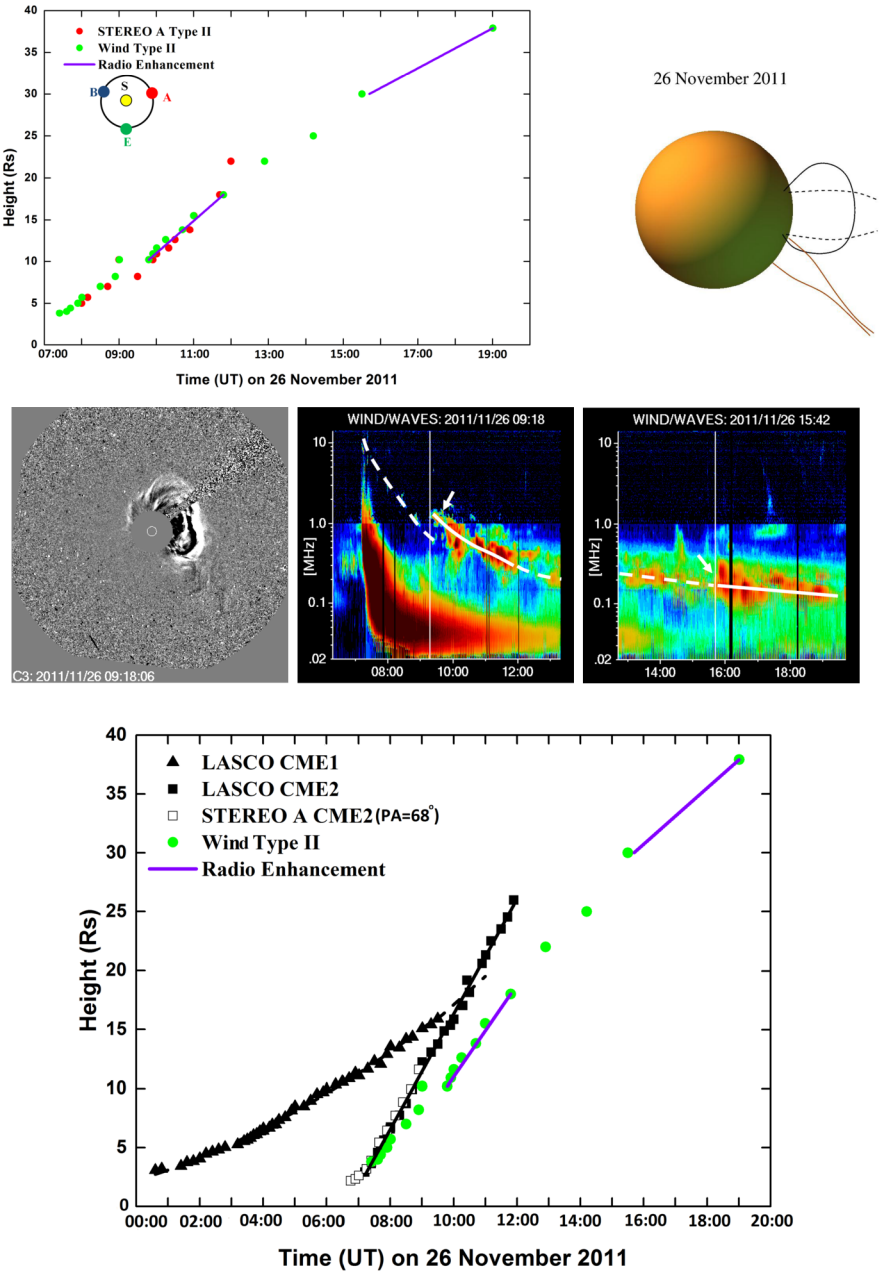

Figure 4 Observed and calculated data for the event on 26 November 2011. *Panels* and *symbols* are the same as in Figure 1.

enhancement) were not necessarily a fundamental–harmonic pair as the frequency ratio was only about 1:1.6 instead of 1:2. The first type II burst had a short duration and fast drift rate, suggesting that it was formed in another region compared with the next two bursts.

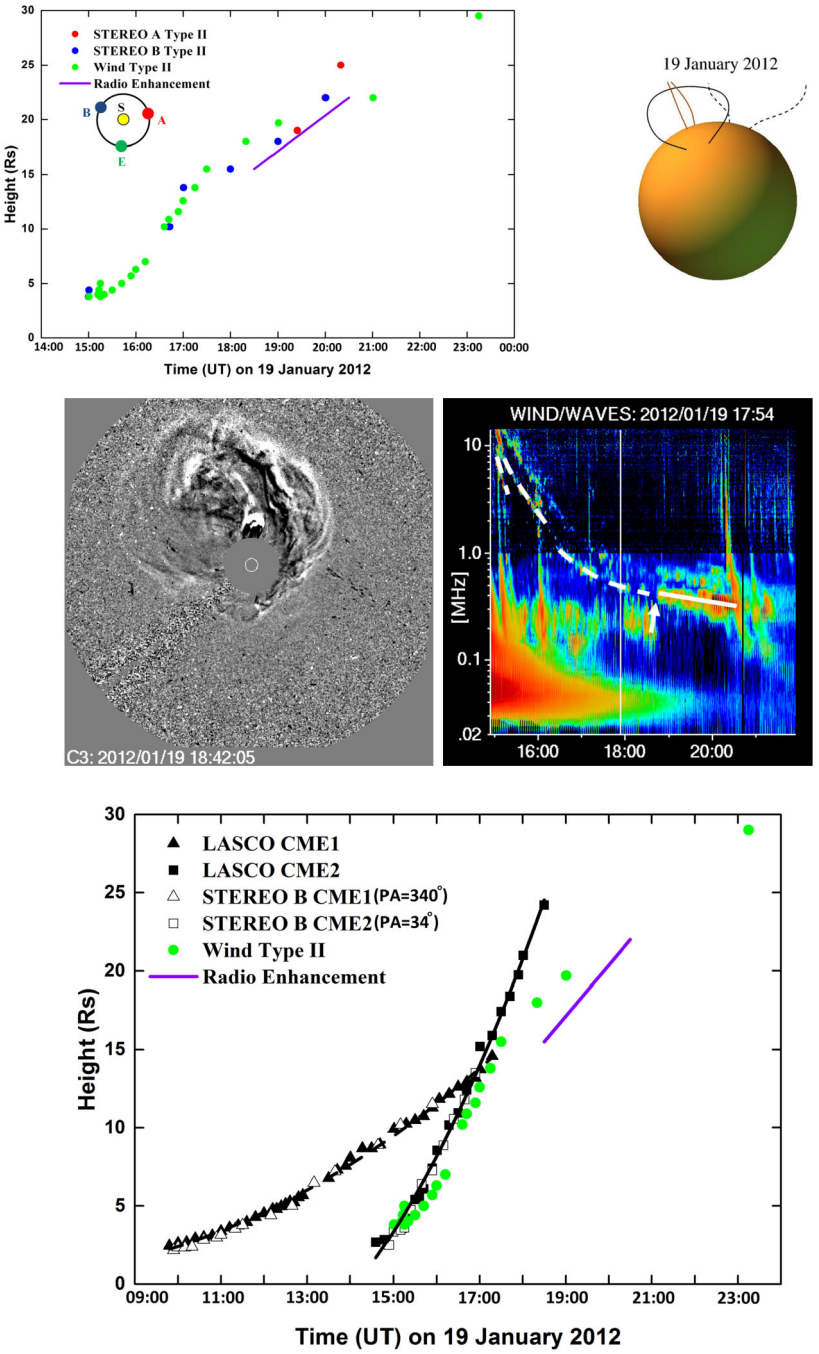

Figure 5 Observed and calculated data for the event on 19 January 2012. *Panels* and *symbols* are the same as in Figure 1.

Similar shocks related to different CME structures have been reported by, *e.g.*, Bemporad and Mancuso (2010).

The radio enhancement started at a height of 15.5 $R_\odot$. The highest CME2 speed reported by Liu *et al.* (2013) occurred very near that time and that height, after which CME2 decelerated. The comparison of CME leading-edge distances derived from triangulation and the radio type II burst heights obtained using the Leblanc density model that were presented in Figure 5 of Liu *et al.* (2013) shows a similar evolution as in our height–time plot for this event: the type II burst follows the CME2 leading front until about 19 UT, after which the type II slows down and falls behind the CME2 front. Near 21 UT, the type II burst heights again approach the CME front heights. The radio enhancement we have analysed here showed most intense emission during the fall-behind period, at 19 – 21 UT, suggesting that the radio enhancement was a separate emission source compared to the type II burst(s).

We conclude that the first three parts of the type II burst were created in different locations, but near the leading front of CME2. The fourth type II part, with enhanced emission, was most probably due to the merging process of the two CMEs, after which the type II burst was again observed near the leading front of the merged CME.

2.2.6. Radio Event 6: 23 January 2012

The halo CME2 (Figure 6) originated from the same active region as the CME2 on 19 January (event 5), but the active region had now rotated to the north-western hemisphere. The CME2 was associated with a long-duration M8.7 class flare. The linear fit from the LASCO observations gives a speed of 2175 km s^{-1}. Using flux-rope and cone-model fits, Xie *et al.* (2013) have also obtained speeds of 2002 km s^{-1} and 2456 km s^{-1}, respectively. These numbers are similar to the speed obtained by Möstl *et al.* (2014) as the CME propagation speed in the IP medium, at the apex of the front. Liu *et al.* (2013), on the other hand, used a triangulation technique on STEREO data and reported a peak speed of about 1600 km s^{-1}. Their speed profiles show impulsive acceleration up to about 16 $R_\odot$ (until about 06:00 UT) and then rapid deceleration for about ten hours, out to about 75 $R_\odot$. The CME heights measured by us using STEREO A data are similar to those obtained with LASCO.

The CME2 was preceded by two CMEs propagating roughly in the same direction. The first, a slow and narrow CME, was first detected at 23:12 UT on 22 January. This CME was associated with a filament eruption near Active Region 11407. The second, a fast and wide CME, was launched from the same active region as CME2 at 03:12 on 23 January. This CME was selected as CME1, but it was already overshadowed by CME2 at a height of 6 $R_\odot$.

The type II burst started with very fragmented and narrow-band emissions, observed by WAVES and SWAVES A during 04:00 – 05:00 UT. The burst then continued as a single wide-band lane, observed only by WAVES. Radio enhancements started to appear within this wide-band lane after 09:00 UT, and some of them were observed by SWAVES A and B as faint emissions. The most intense radio enhancement occurred at low frequencies, below 250 kHz, after 12:35 UT. This corresponds to a height of about 25 $R_\odot$. We note that our height calculations were made using the wide-band lane centre, which may cause considerable uncertainty in the height estimation. The height comparison between CME leading-edge distances from triangulation and the radio type II burst heights obtained using the Leblanc density model, reported by Liu *et al.* (2013) and shown in their Figure 10, suggests that the type II burst may have been located at the CME leading front all the time. However, their error margins for the type II heights, based on the emission bandwidths, are large, >30 $R_\odot$. By using the maximum frequency range estimated for the second part of

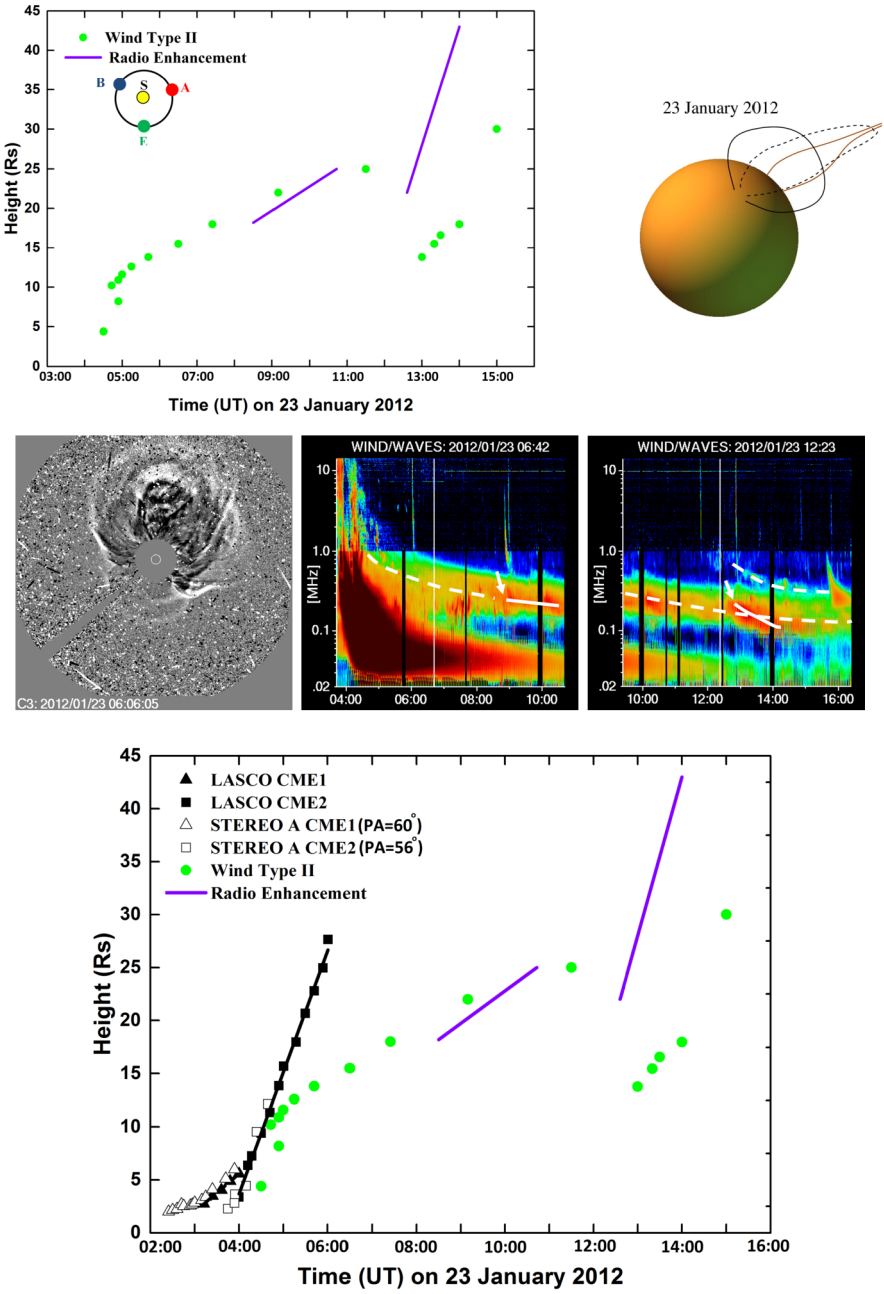

Figure 6 Observed and calculated data for the event on 23 January 2012. *Panels* and *symbols* are the same as in Figure 1. The LASCO C3 image is from 06:06 UT, about two hours before the start of the first radio enhancement. This is because of the intense particle hits in the later LASCO images.

type II burst after 12:35 UT (see Table 3), we obtain an error margin of ~ 20 $R_\odot$ for the radio height from the hybrid density model.

The radio spectrum also shows a narrow-band frequency-drifting type II-like feature above the wide-band type II burst during 13 – 15 UT. It had a start frequency of 600 kHz, indicating a height of 14 $R_\odot$ if it was the fundamental emission lane. It is highly improbable that any of the earlier CMEs would have been at that height with a speed capable of creating a shock. If, however, the emission was harmonic (the fundamental lane being overshadowed by the wide-band lane), then the source height would have been much higher, ~ 22 $R_\odot$ (300 kHz). The radio enhancement could in this case be due to observing two different shocks that were not necessarily connected to each other.

We conclude that the radio enhancements within the wide-band type II burst lane may have several different origins.

2.2.7. Radio Event 7: 5 March 2012

The halo CME2 (Figure 7) originated from the north-eastern hemisphere and was associated with an X1.1 class flare. The earlier CME1 originated from the same active region and was associated with the same flare, as the flare had two maxima, and it continued several hours after the CME2 launch time.

The linear fit from the LASCO observations gives CME2 a speed of 1532 km s^{-1}. Möstl *et al.* (2014) used croissant modelling to estimate the initial speed and obtained a speed of 974 km s^{-1}, but the IP propagation speed was determined to be higher, 1347 km s^{-1}. CME1 was much slower, with a linear fit speed of 594 km s^{-1}.

SWAVES B observed a clear fundamental–harmonic pair of type II emission lanes during 04:00 – 06:00 UT, but during this period, WAVES and SWAVES A saw only sporadic type II emission. At 06:30 UT, enhanced radio emission was observed to start below the height of the type II lane. A second enhancement appeared one hour later, now along the type II lane, but also at lower frequencies, and showing wide-band emission. All these radio burst sources had much lower heights than those of the observed CME2 leading front.

This event has been analysed by Magdalenić *et al.* (2014) using the radio triangulation technique. Their results indicated that the source of the type II burst was situated on the southern flank of CME2. However, the source heights from triangulation did not match any atmospheric density model, as they were 10 – 20 $R_\odot$ higher than expected. Magdalenić *et al.* (2014) suggested that the interaction of a shock wave and the nearby coronal streamer resulted in the interplanetary type II radio emission. On closer inspection, we discovered that the triangulated heights were a direct continuation of the LASCO CME2 leading front heights. However, this discovery does not explain the high frequency of the emission, which must either rise from dense plasma or be created by some unknown plasma process.

We therefore conclude that there are two possibilities for the enhanced emission. Either the emission was created at the CME2 leading front when the shock propagated to very high-density plasma, or the emission was due to CME–streamer interaction at lower heights.

2.2.8. Radio Event 8: 10 March 2012

The halo CME2 (Figure 8) originated from the north-western hemisphere and was associated with an M8.4 class flare. The linear fit from the LASCO observations gives a speed of 1296 km s^{-1}. The flux-rope model fit by Xie *et al.* (2013) gave a radial speed of 1705 km s^{-1} and their cone-model fit resulted in 1378 km s^{-1}. The IP propagation speed determined by Möstl *et al.* (2014), 1297 km s^{-1}, was very similar to the LASCO linear fit speed, however.

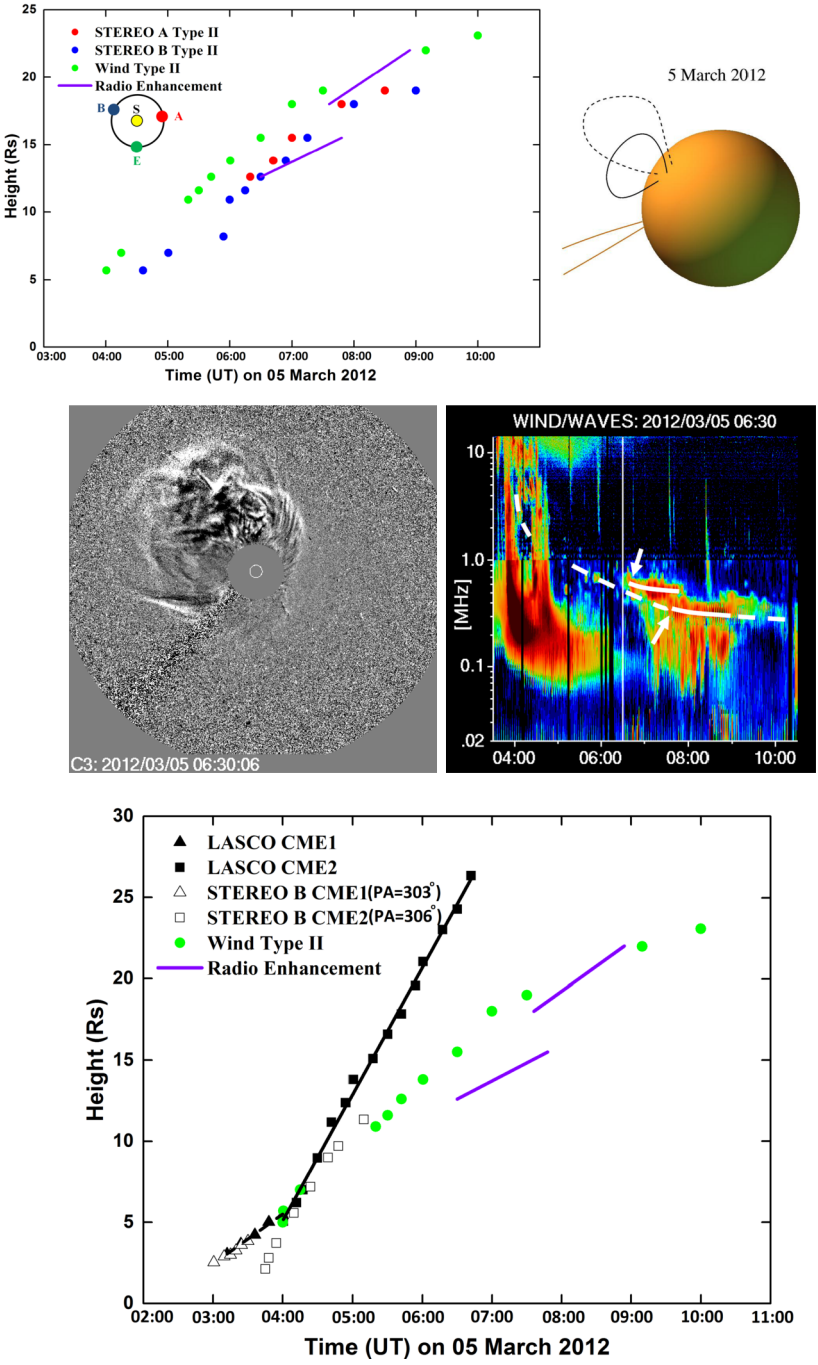

Figure 7 Observed and calculated data for the event on 5 March 2012. *Panels* and *symbols* are the same as in Figure 1.

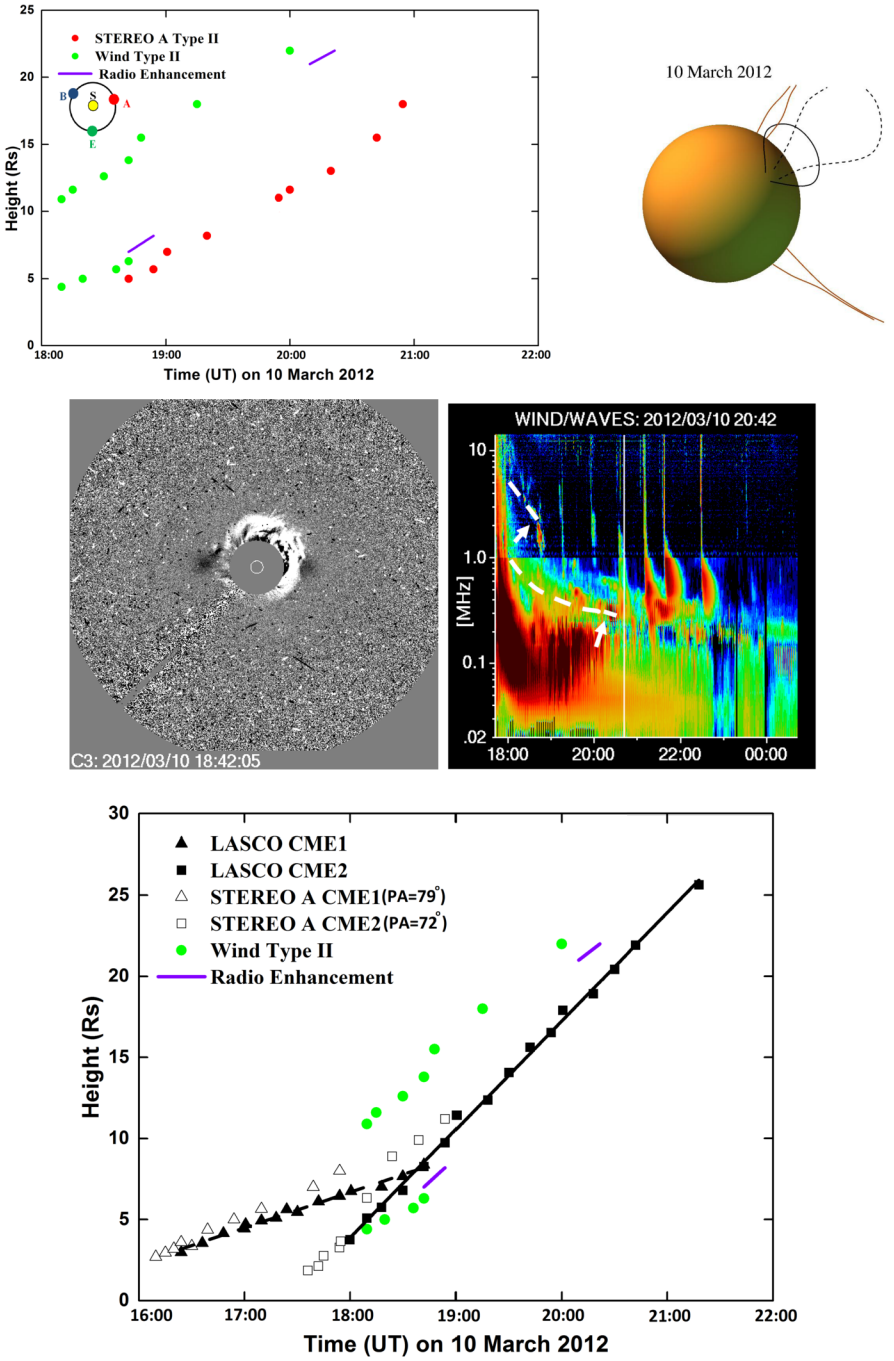

Figure 8 Observed and calculated data for the event on 10 March 2012. *Panels* and *symbols* are the same as in Figure 1.

The earlier CME1 originated from a nearby active region and was associated with a C8.0 class flare. This partial-halo CME was launched about one and a half hours before CME2, and it had a linear fit speed of 423 km s^{-1}.

At metric wavelengths there is some indication of a short-duration type II burst associated with CME1, and the radio event associated with CME2 was also first observed at meter waves. In the IP space, intermittent fundamental and harmonic type II emission was observed by WAVES above 2 MHz, and a separate wide-band emission lane was observed at lower frequencies, below 1 MHz. The first radio enhancement appeared near the type II harmonic lane and the second enhancement in the fundamental lane, which was also inside the wide-band lane. SWAVES A showed only type II emission patches, but no wide-band emission. SWAVES B did not observe any of these structures.

The CME fronts reached the same heights at about 18:15 UT, near ~ 7 R$_\odot$, and soon after this, the first radio enhancement was observed. A streamer was also present north of the CMEs, and as the merging of the two CMEs was most probably completed by 20 UT, we conclude that the later radio enhancement within the wide-band type II lane could have been the result of CME–streamer interaction. An unknown origin associated with wide-band emission is also possible, however.

2.2.9. Radio Event 9: 17 May 2012

The halo CME2 (Figure 9) originated from the western hemisphere and was associated with an M5.1 class flare. The linear fit from the LASCO observations gives a speed of 1582 km s^{-1}, but STEREO observations provided a slightly slower speed of 1302 km s^{-1} (Papaioannou *et al.*, 2014; this article mainly describes the particle event GLE71 that followed the eruption). Streamers were observed on both sides of this CME. Our height measurements from STEREO A data also give a slightly lower CME speed of 1213 km^{-1} compared to LASCO.

An earlier CME1, observed the day before and directed towards the north-east, was not associated with a known flare. The linear fit speed of CME1 was 306 km s^{-1}.

A wide-band radio emission lane was observed by SWAVES A at the event start. After 03 UT, both SWAVES A and WAVES observed multiple emission bands, some of which showed curved frequency drifts and patches of enhanced emission. SWAVES B did not observe any of these emissions, which indicates that the emission source(s) were located in the western or south-western hemisphere.

Even though Figure 9 and Table 2 show very little height difference between the leading fronts of the two CMEs, there is no interaction between these fronts because the CMEs are propagating in clearly different directions. The flank of CME2 does reach the root of CME1 just after 03:00 UT, but no effect is visible in the CME1 structure. Instead, the opposite flank of CME2 collides quite violently with a southern streamer, which is the most probable cause for the enhanced radio emission. As the type II heights are much lower than the CME leading front heights, the type II emitting shock could have been located at the CME2 flanks.

2.2.10. Radio Event 10: 17 July 2012

The partial-halo CME2 (Figure 10) originated from the south-western hemisphere and was associated with a long-duration M1.7 class flare that started almost two hours before the CME. In Hα, two flares were listed to have occurred during that time in the same active region (11520). The linear fit from the LASCO observations gives CME2 a speed of 958 km s^{-1}. We note that streamers were present on both sides of CME2.

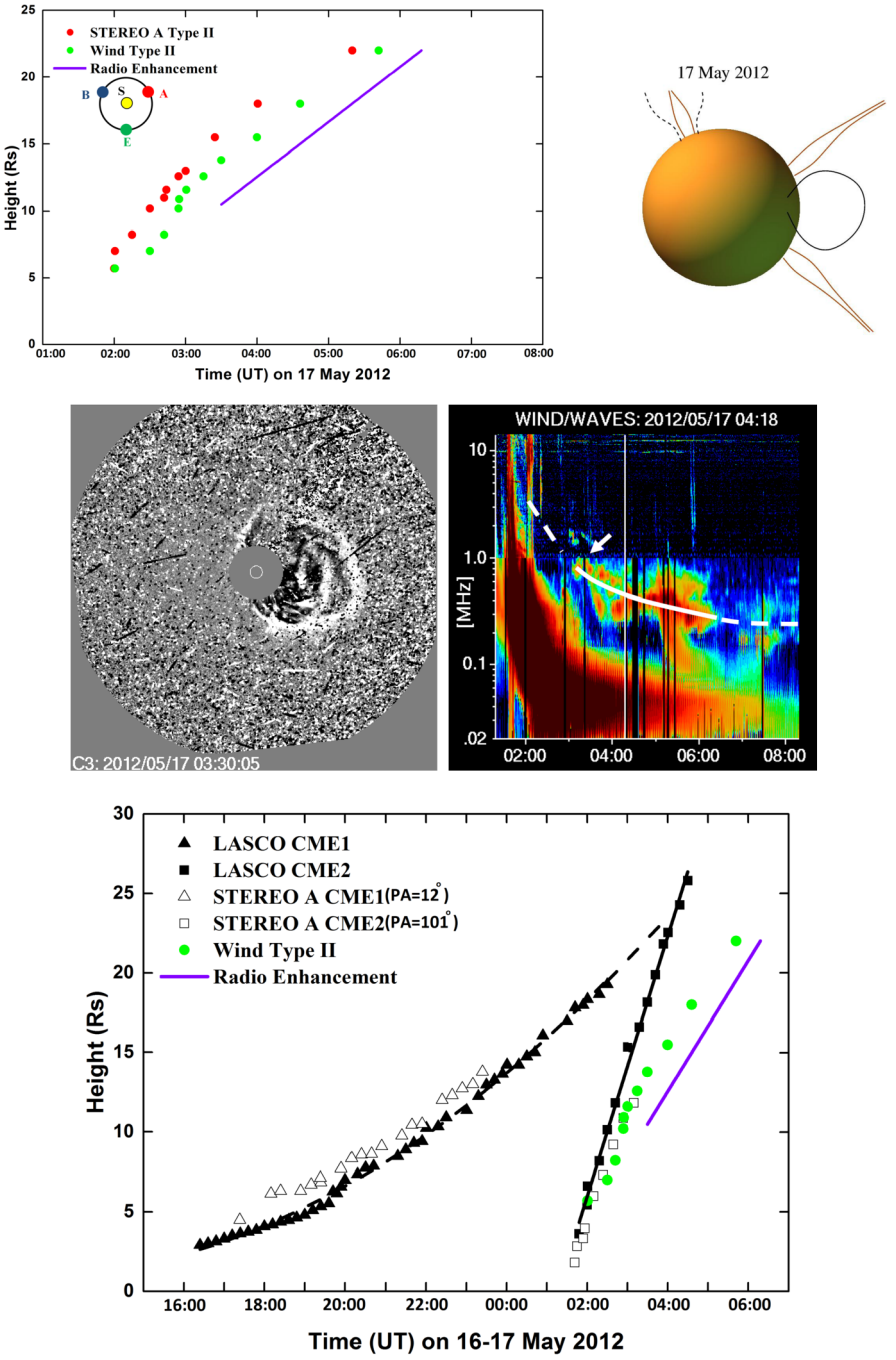

Figure 9 Observed and calculated data for the event on 17 May 2012. *Panels* and *symbols* are the same as in Figure 1.

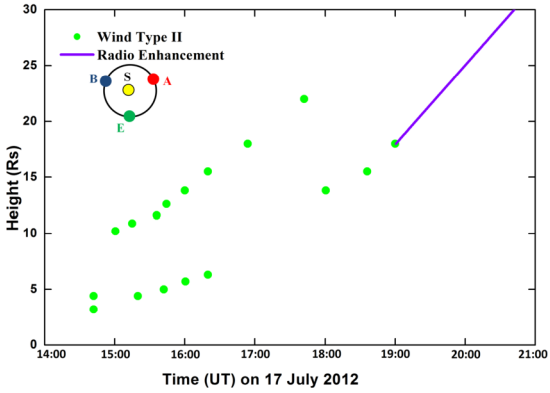

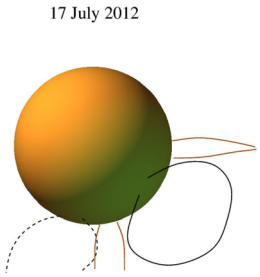

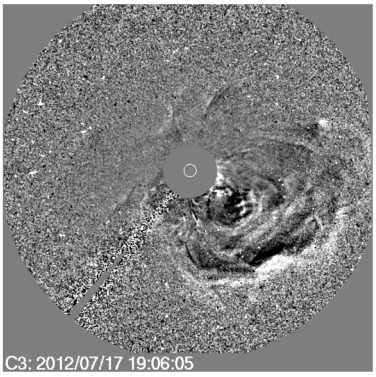

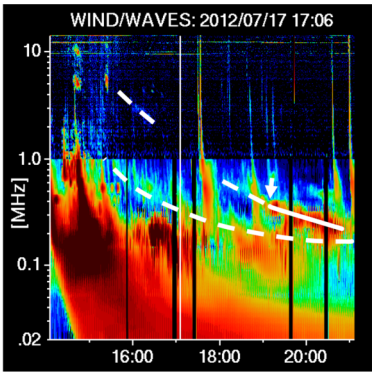

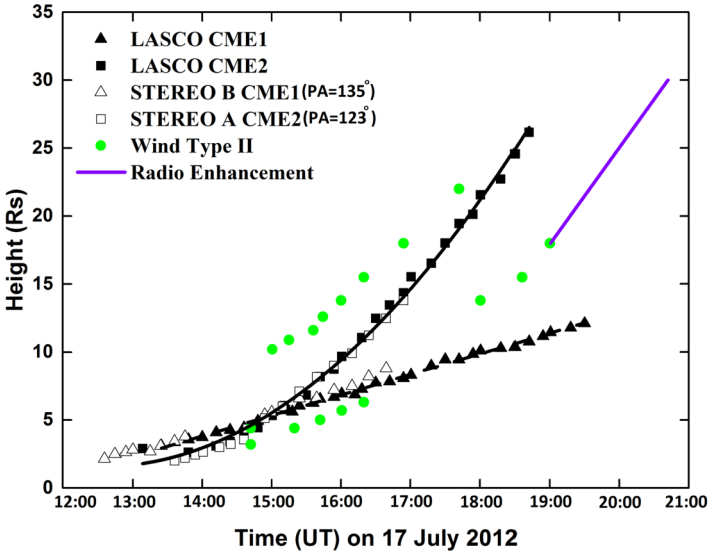

Figure 10 Observed and calculated data for the event on 17 July 2012. *Panels* and *symbols* are the same as in Figure 1.

The earlier CME1 was first observed 23 minutes before the first observation of CME2; they therefore appeared very close in time. CME1 was directed towards the south-east, and it had a different source region than CME2. The linear fit speed of CME1 was 292 km s^{-1}.

The type II burst emission starts at 14:40 UT, which is about one hour after CME2 was first observed. A fundamental–harmonic pair is visible for a short period, after which short sporadic emission patches are observed. The start of the burst is observed by both WAVES and SWAVES A. When the burst continues to frequencies below 1 MHz, it is no longer clear if the two emission lanes are a continuation of the same type II burst. This later emission is observed only by WAVES.

The leading fronts of both CMEs are still observed after they have reached the same heights, which also shows that the two CMEs are propagating in different directions. Thus there is no interaction between these CMEs. The CME heights are also confirmed by the SECCHI A and B observations. The two type II emission lanes could be due to a simultaneous CME2 bow shock and a shock at the flanks of CME2. The radio enhancement could then be created by streamer–CME flank shock interaction.

2.2.11. Radio Event 11: 31 August 2012

The halo CME2 (Figure 11) originated from the south-eastern hemisphere and was associated with a long-duration C8.4 class flare that was also associated with a large-scale filament eruption. The linear fit from the LASCO observations gives a speed of 1442 km s^{-1}.

The earlier CME1 originated from a nearby active region and was associated with flaring. The C1.3 class X-ray flare listed in Table 1 occurred at a time when CME1 was already at a height of 3 $R_{\odot}$ and a C1.9 flare before this had already ended when CME1 was estimated to have been launched. The CME1 was launched some nine hours before CME2, and it had a linear fit speed of 706 km s^{-1}.

The WAVES and SWAVES B radio dynamic spectra show intermittent type II emission at fundamental and harmonic frequencies associated with CME2. SWAVES A does not observe any of this emission. The radio enhancements after 22:00 UT appear within the fundamental emission lane, and the emission lane observed by WAVES changes into wide-band emission the next day. The type II burst heights are lower than the CME2 heights almost from the start, and it seems very unlikely that CME1 could have affected the propagation of CME2 or the associated shock. Most likely, the radio enhancements were caused by CME flank shock–streamer interaction.

2.2.12. Radio Event 12: 15 March 2013

The halo CME2 (Figure 12) originated from the north-eastern hemisphere but almost from the disk centre, and it was associated with an M1.1 class flare. The linear fit from the LASCO observations gives a speed of 1063 km s^{-1} and the speed derived from the STEREO coronagraph observations is very similar (Wu *et al.*, 2016).

The closest-in-time CME that originated from the same hemisphere and was large/intense enough to have affected the propagation of CME2 occurred more than two days before (on 12 March, first observed at 23:48 UT).

Type II burst emission was observed only by WAVES, and the continuous (identifiable) emission started when the CME had already propagated outside the LASCO C3 field of view. During 11 – 13 UT, one single and relatively wide emission lane was observed at 300 – 450 kHz. At about 13 UT, a more narrow frequency-drifting lane appeared below it, starting at 250 MHz. The two emission lanes observed at 14 – 15 UT had a frequency ratio of almost

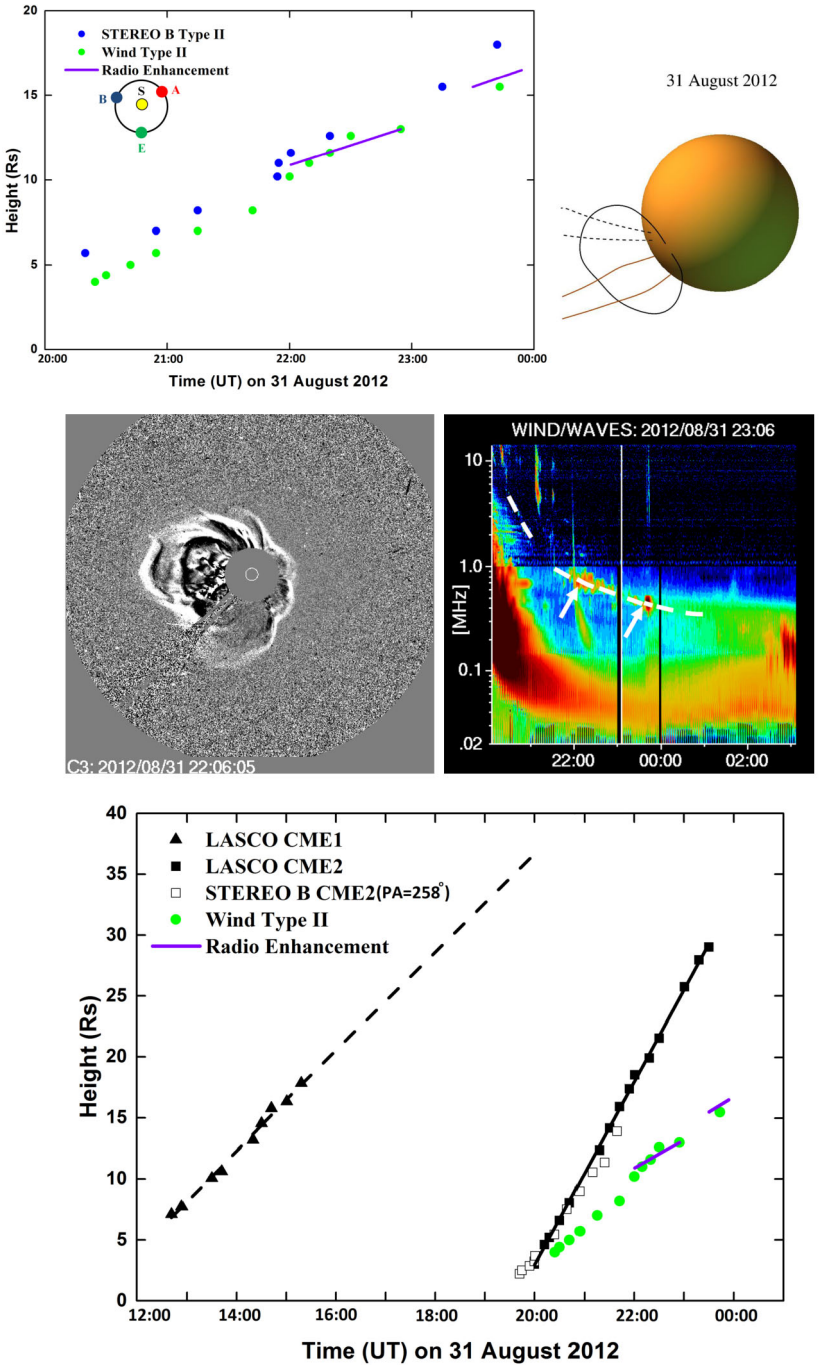

Figure 11 Observed and calculated data for the event on 31 August 2012. *Panels* and *symbols* are the same as in Figure 1.

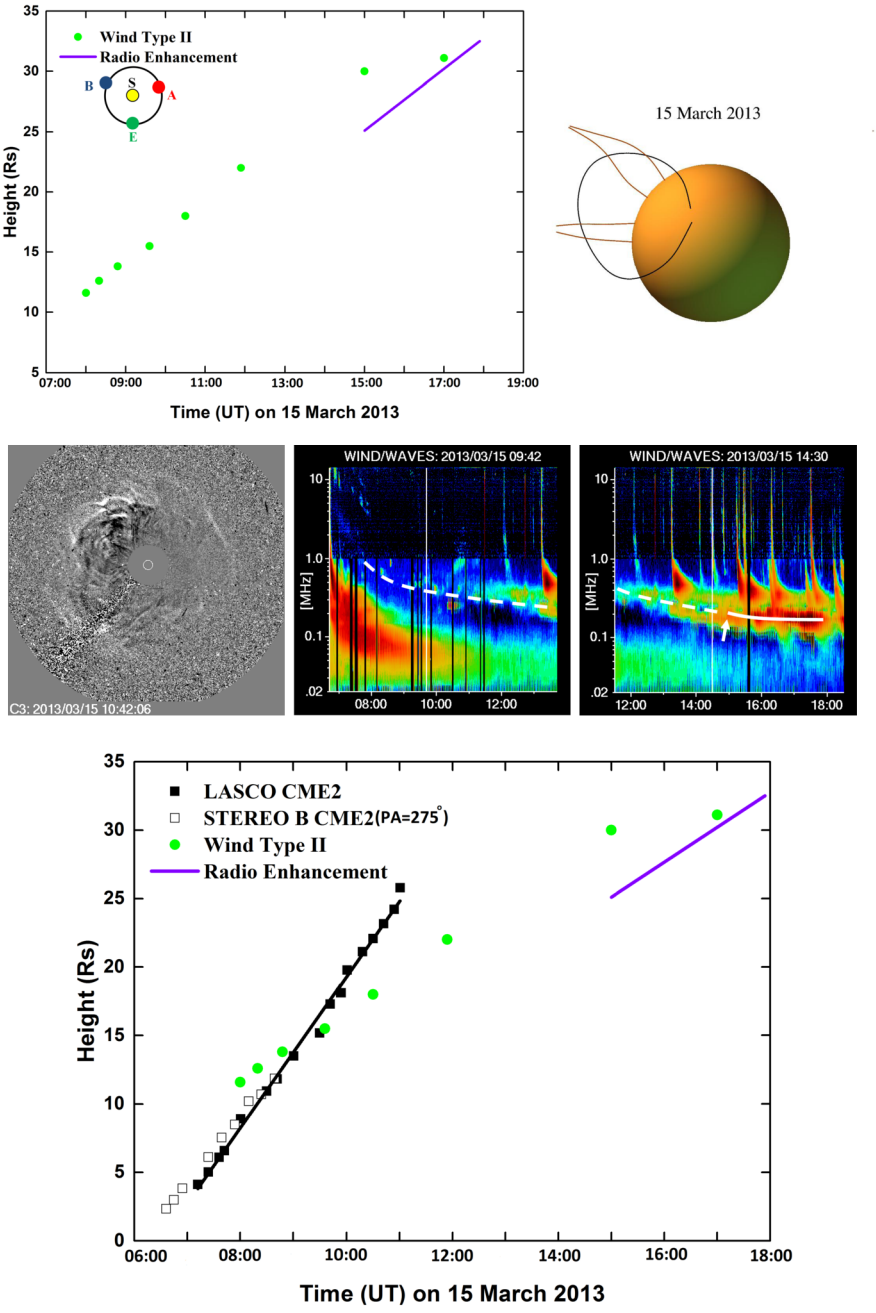

Figure 12 Observed and calculated data for the event on 15 March 2013. *Panels* and *symbols* are the same as in Figure 1. The LASCO C3 image is from 10:42 UT, about four hours before the start of the radio enhancement.

1:2, suggesting possible fundamental–harmonic emission. Near 15:00 UT, strong enhanced emission was observed to start within the lower emission lane, and at the same time, type III bursts were seen to stop near the upper emission lane.

The ending of the type III bursts at a certain frequency indicates that the electron beams could not propagate further. These electrons could serve as an additional source of particles, leading to the observed enhanced density signature when the shock wave passes through the region. Alternatively, the radio enhancement could be due to the overlap of the type II and type III emissions. The fact that there is a gap between the end frequencies of the type III bursts and the enhanced type II lane contradicts this interpretation.

2.2.13. Radio Event 13: 22 May 2013

The halo CME2 (Figure 13) originated from the north-western hemisphere and was associated with an M5.0 class flare. The linear fit from the LASCO observations gives a speed of 1466 $\mathrm{km\,s^{-1}}$. The peak speed of CME2 was determined by Ding *et al.* (2014) to be 1800 $\mathrm{km\,s^{-1}}$.

The earlier CME1 originated from the same active region and was associated with a C2.3 class flare. The CME was a partial halo with a linear speed of 687 $\mathrm{km\,s^{-1}}$, although the fit made by Ding *et al.* (2014) gives a lower speed of 519 $\mathrm{km\,s^{-1}}$.

The radio type II burst associated with CME2 was very intense and complex, showing both fundamental and harmonic emission. The type II radio emission was observed by all three radio instruments, SWAVES A, SWAVES B, and WAVES.

Ding *et al.* (2014) used a graduated cylindrical shell model to reconstruct the propagation of the two CMEs. They found that the leading edge of the second CME (CME2) caught up with the trailing edge of the first CME (CME1) at a height of about 6 $\mathrm{R_\odot}$, and after about two hours, the leading edges of the two CMEs merged at a height of about 20 $\mathrm{R_\odot}$. The type II burst showed strong enhancement during this two-hour period. Mäkelä *et al.* (2016) used a direction-finding technique in the analysis of the radio burst and concluded that the source of the radio enhancement was CME–CME interaction. They found that the radio source locations at 800 – 1000 kHz were near the CME leading front (*i.e.* just before the radio enhancement start). However, at frequencies lower than 800 kHz (where most of the radio enhancements appeared), triangulation gave unrealistically large height values.

Our Figure 13 (lower panel) shows that the calculated heights for the radio enhancement remain below the CME2 leading front. This suggests that the emission was created within dense plasma, located higher than the atmospheric density models would give. The wide frequency range of the radio emission also suggests that the source was the merging of the plasma from the two CMEs.

2.2.14. Radio Event 14: 29 September 2013

The halo CME2 (Figure 14) originated from the north-western hemisphere. It was associated with a large-scale filament eruption and a long-duration C1.2 class X-ray flare. The linear fit from the LASCO observations gives CME2 a speed of 1179 $\mathrm{km\,s^{-1}}$.

The only CME that could have affected the propagation of CME2 was observed eight hours earlier, moving towards the south with a linear fit speed of 374 $\mathrm{km\,s^{-1}}$. Near this CME1 launch time, a C1.6 class X-ray flare occurred at N18W87, but it seems highly improbable that it was associated with CME1 because of the distant location.

The type II burst associated with CME2 showed fragmented emission at the start and a more continuous enhancement from 00:12 onwards on 30 September. These bursts were

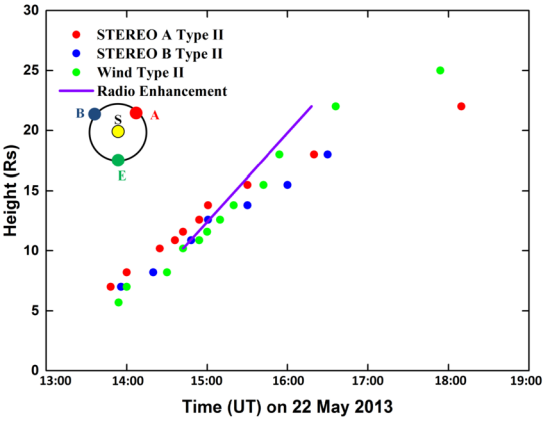

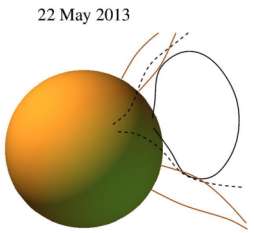

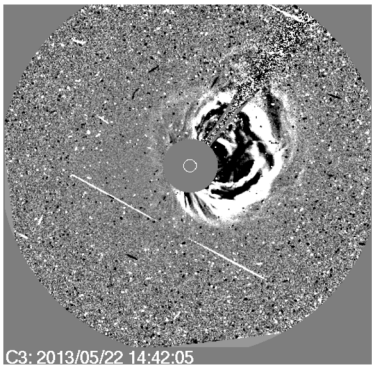

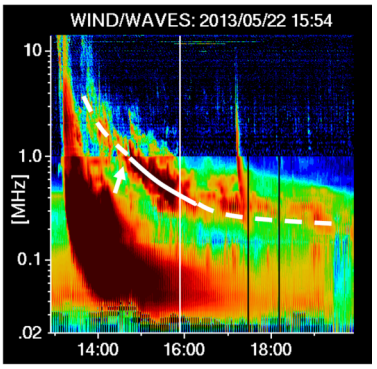

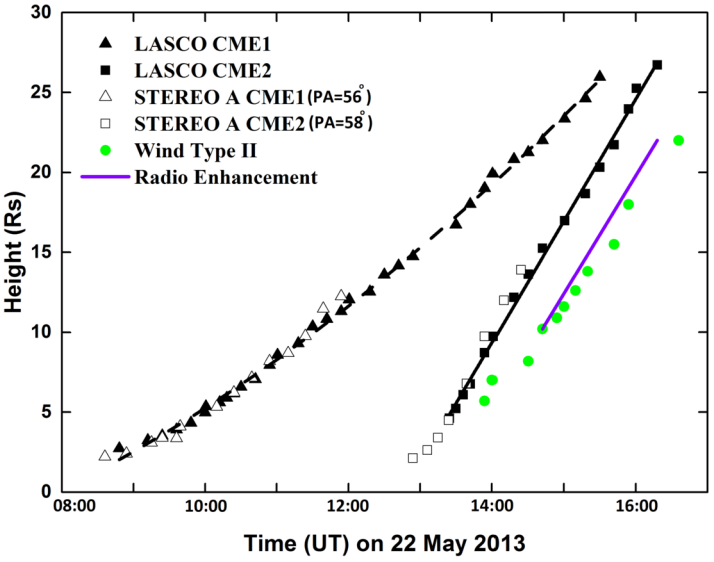

Figure 13 Observed and calculated data for the event on 22 May 2013. *Panels* and *symbols* are the same as in Figure 1.

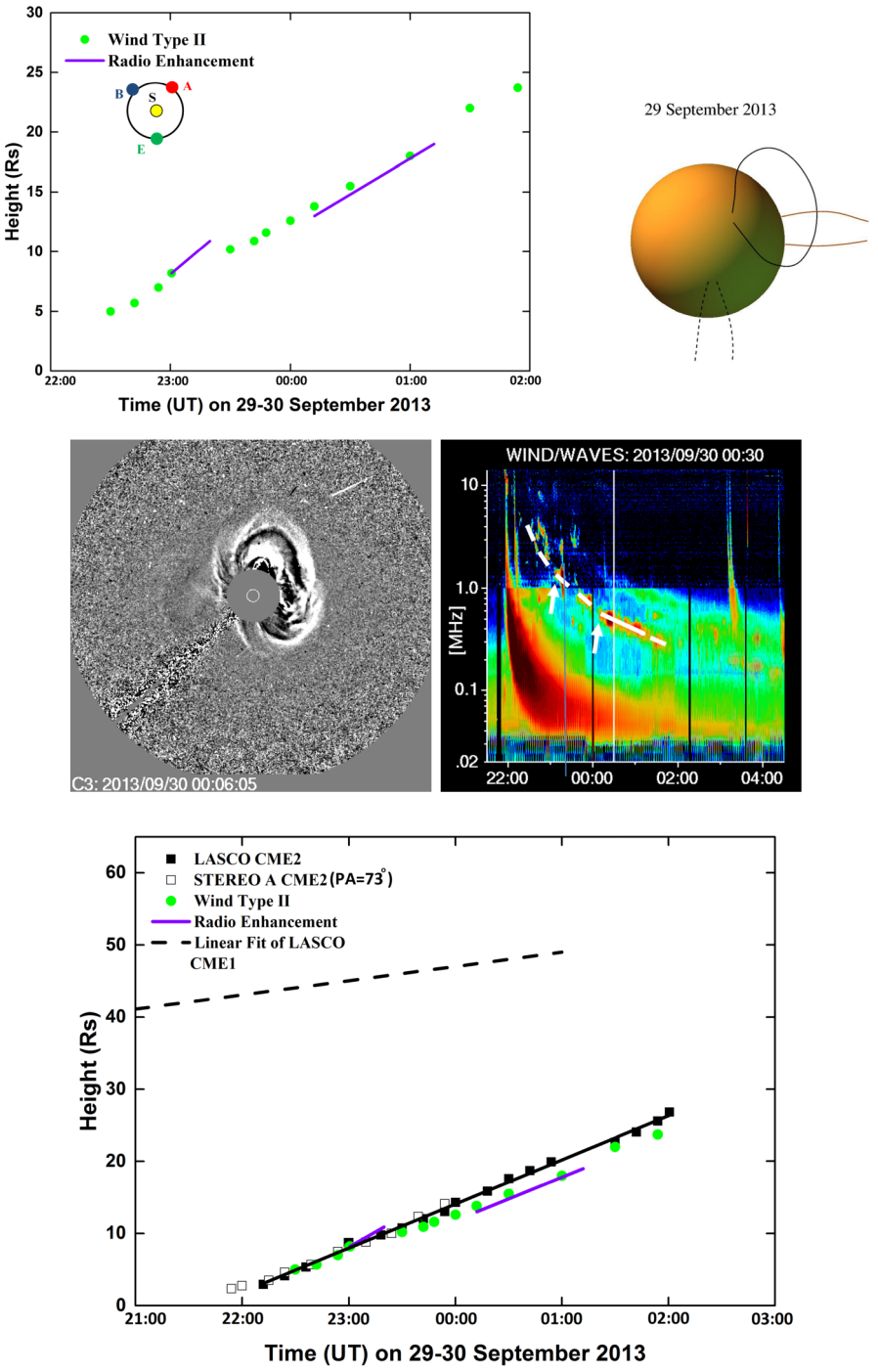

Figure 14 Observed and calculated data for the event on 30 September 2013. *Panels* and *symbols* are the same as in Figure 1.

mainly observed by WAVES, while SWAVES A and B observed only faint emission. The radio enhancement was located along the type II lane, and it was quite narrow-band. The radio enhancement heights are very near the CME leading front heights, and therefore we suggest that the enhancements were created when the CME2 bow shock propagated through plasma from earlier transients.

2.2.15. Radio Event 15: 7 January 2014

The halo CME2 (Figure 15) originated from the south-western hemisphere and was associated with an X1.2 class flare near the disk centre, located between Active Regions 11943 and 11944. The linear fit from the LASCO observations gives a speed of 1830 km s^{-1}. The speed of this CME has also been determined with a graduated cylindrical shell model (Möstl *et al.*, 2015) and with a WSA–ENLIL+Cone ensemble model (Mays *et al.*, 2015), and the obtained speeds were $\approx$ 2500 km s^{-1}. The CME had a non-radial propagation direction, as it originated from a region in the disk centre and a significant geomagnetic impact was forecast, but only minimal effects were recorded. Möstl *et al.* (2015) concluded that the change in direction was attained very close to the Sun, < 2.1 R$_\odot$.

The earlier partial halo-type CME that could have affected the propagation of CME2 occurred 15 hours before. The source region of the earlier CME was behind the western limb at about S15W125. Because of the time difference and source locations, we estimate that there was most probably no interaction between these two CMEs.

CME1 was not associated with an IP type II burst. The type II burst associated with CME2 was observed by WAVES as a wide-band emission lane. SWAVES A and B both observed a strong narrow-band type II burst during 20:00 – 22:00 UT, with a faint harmonic band visible as well. The height–time plot of the type II burst shows very different height values measured from the WAVES spectrum and from the SWAVES A and B spectra. This may be due to the different bandwidths of the type II lanes, or to the STEREO A and B spacecraft positions on the backside of the Sun, with limited view towards the CME propagation.

We conclude that the wide-band emission, with enhanced emission patches within the lane, originated from a source (or emission mechanism) that was directed towards Earth. We note that in this propagation direction a streamer was also present.

2.2.16. Radio Event 16: 18 April 2014

The halo CME2 (Figure 16) originated from the south-western hemisphere and was associated with an M7.3 class flare. The linear fit from the LASCO observations gives a speed of 1203 km s^{-1}.

The earlier CME1 that could have affected the propagation of CME2 was launched about five hours earlier, in the same direction as CME2 and with a linear fit speed of 387 km s^{-1}. The CME1 was associated with a C1.6 class X-ray flare in the same active region.

The type II burst associated with CME2 showed intermittent emission at fundamental and harmonic frequencies, observed only by WAVES. Later, after 17:30 UT, the emission was observed to have a broader band and only one lane.

The radio enhancements appear at a time when the height separation of the leading edges of the two CMEs is about 4.5 R$_\odot$, suggesting that this is the time when the leading front of CME2 meets the rear end of CME1. The start of the broader-band one-lane emission could indicate that then the CMEs merged.

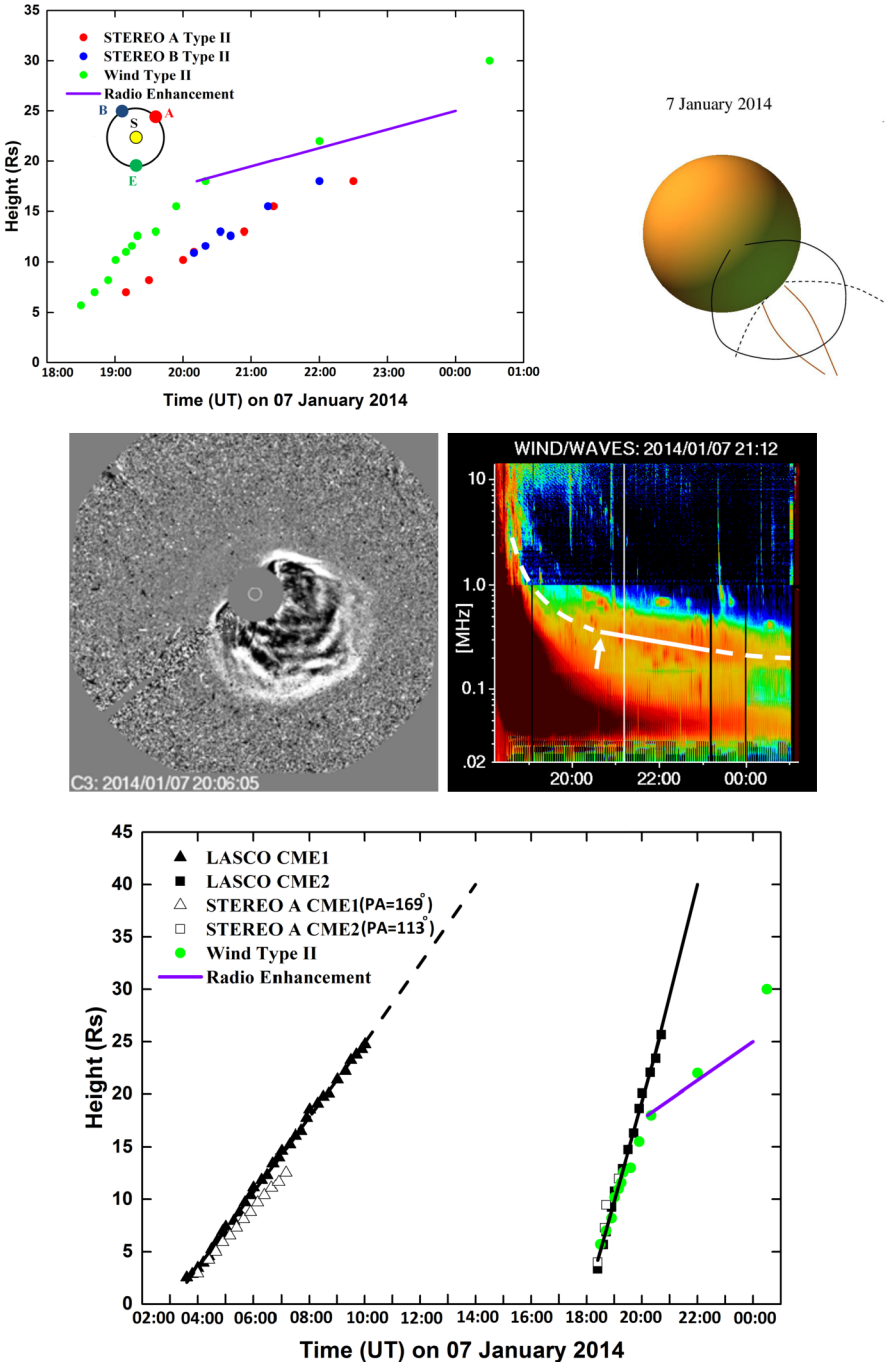

Figure 15 Observed and calculated data for the event on 07 January 2014. *Panels* and *symbols* are the same as in Figure 1.

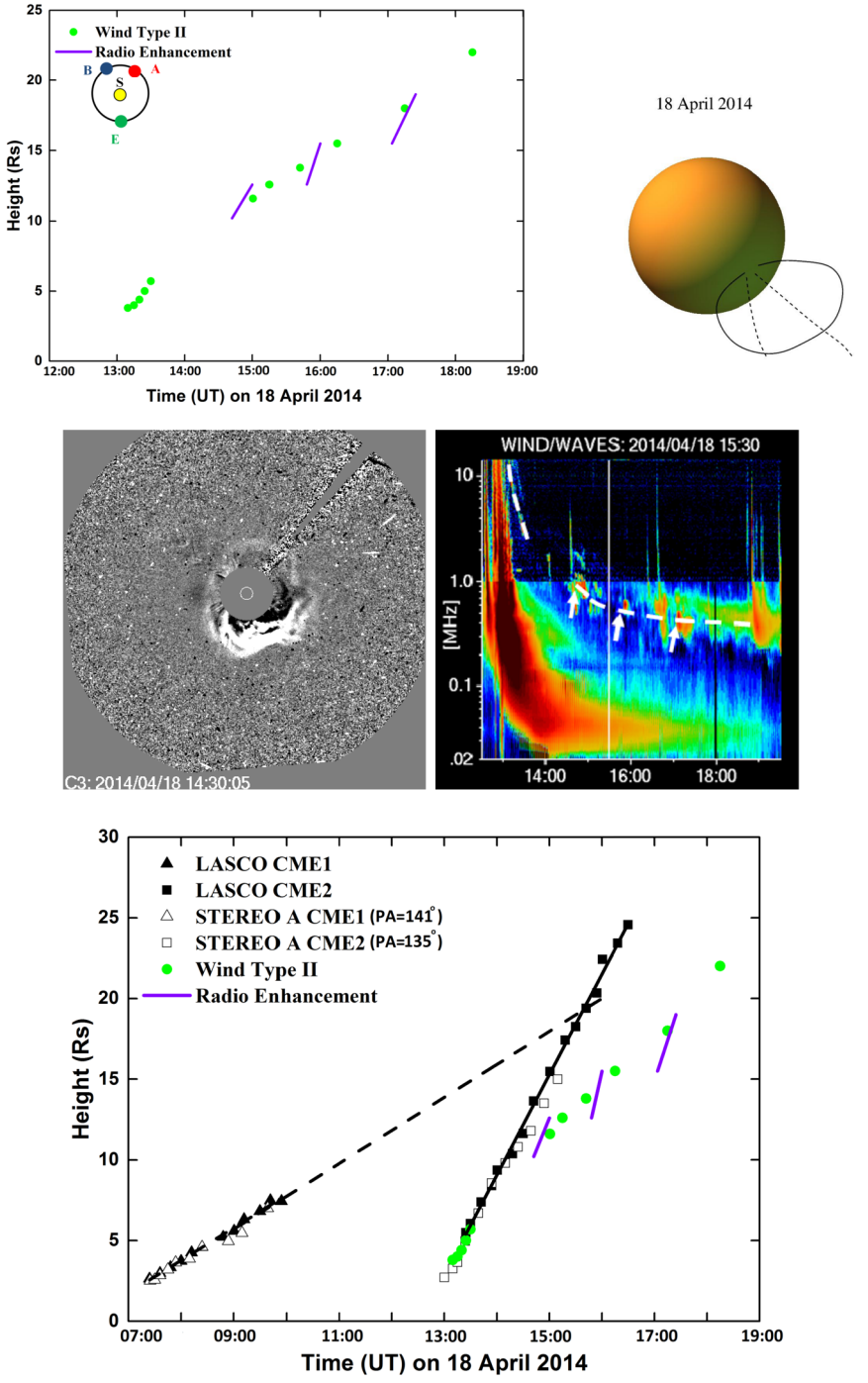

Figure 16 Observed and calculated data for the event on 18 April 2014. *Panels* and *symbols* are the same as in Figure 1.

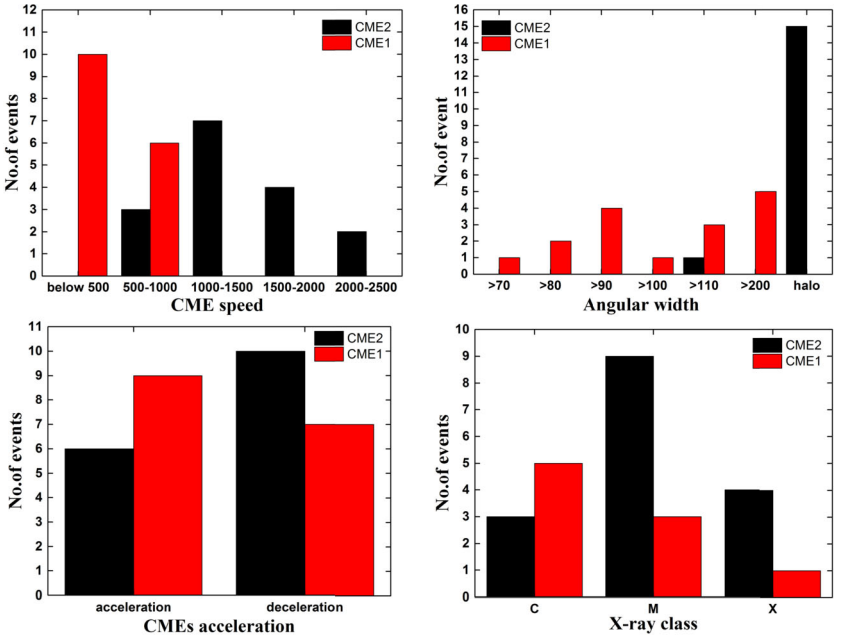

Figure 17 CME and flare characteristics for the investigated 16 events. CME2 (*black*) is the primary CME event, and CME1 (*red*) is the earlier CME event.

2.3. CME and Flare Characteristics

The 16 events from 2011 – 2014 we analysed occurred close to the solar maximum, and all the primary CMEs except for one were full halos, the exception being a partial halo with an angular width of 176°. These CMEs had very high speeds (1063 – 2175 km s^{-1}), with only three CMEs having speeds slower than this (669 – 958 km s^{-1}), see Table 1 and Figure 17. The primary CMEs were also associated with intense X-ray flares: four X-class, nine M-class, and three C-class.

The preceding CMEs that could have played a role in the formation of the radio enhancements had much lower speeds in general, 10 out of the 16 had a speed below 500 km s^{-1}, the lowest recorded speed being 229 km s^{-1}. The six faster CMEs had speeds of 594 – 706 km s^{-1} (Table 1). Nine of these CMEs were observed with X-ray flaring: one was X-class, three were M-class, and five were C-class (of which one had an uncertain association with that particular CME because of the large time difference between the two). Seven of the CMEs had no clear association with an X-ray flare, but some of them showed flaring in Hα.

Because fast and wide CMEs are typically more likely to produce type II radio bursts and because our first selection criterion was to find type II bursts with radio enhancements, the outcome of having high-speed halo/partial-halo CMEs associated with our radio events is no surprise. Eleven out of the 16 events also produced solar energetic particles (SEPs), which confirms that particle acceleration also occured during CME propagation.

2.4. Characteristics of the Radio Enhancements

We summarise the measured characteristics of the radio enhancements in Table 3: duration, average bandwidth, maximum instantaneous frequency range of emission, and average drift

Table 3 Characteristics of the radio enhancements. Durat. is the total duration of the radio enhancement, and Cat. is the derived burst category.

No.	Date	Start time UT	Durat. hh:mm	Band-width kHz	Max. range kHz	Drift kHz s^{-1}	Type III	Low freq. ext.	Cat.
1	15 Feb. 2011	04:48	01:00	350	600	0.160	Yes		1(5)
2	08 Mar. 2011	00:06	01:54	100	250	0.036		Yes	3
3	22 Sep. 2011	16:19	01:00	120	270	0.075			3
4	26 Nov. 2011	09:18	02:48	700	900	0.120			2
		15:42	03:37	180	310	0.023			3
5	19 Jan. 2012	18:41	01:48	150	250	0.038			2
6	23 Jan. 2012	08:20	02:14	150	450	0.055			4
		12:25	02:25	100	210	0.024			4
7	05 Mar. 2012	06:30	01:18	260	500	0.100		Yes	3(1)
		07:36	01:18	120	250	0.053			3(1)
8	10 Mar. 2012	18:42	00:12	280	700	0.130			1
		20:18	00:14	100	150	0.170			4
9	17 May 2012	03:30	03:24	140	600	0.150	Yes	Yes	3(5)
10	17 Jul. 2012	19:06	01:36	120	250	0.043			3
11	31 Aug. 2012	22:06	00:54	140	350	0.100			3
		23:33	00:20	160	200	0.160			3
12	15 Mar. 2013	15:00	02:54	80	160	0.015	Yes		5
13	22 May 2013	14:42	01:36	320	1200	0.390			2
14	29 Sep. 2013	23:06	00:16	480	800	0.666			1
		00:12	01:00	100	400	0.110			1
15	07 Jan. 2014	20:06	03:54	180	750	0.053			4
16	18 Apr. 2014	14:42	00:36	190	300	0.130			2
		15:51	00:07	140	200	0.010			2
		17:07	00:25	180	220	0.140			2

Category 1: Enhancement superposed on type II burst lane.

Category 2: CME–CME interaction.

Category 3: CME flank–streamer interaction.

Category 4: Enhancement within wide-band type II emission.

Category 5: Enhancement with type III burst association.

rate. The table also contains information regarding whether type III burst activity was observed during the enhancement and if there was a low-frequency extension in the emission.

We divided the radio enhancements into five different categories, depending on their characteristics and the information obtained from our analysis. The category numbers, 1 – 5, are also shown in Table 3.

In category 1 events, the radio enhancements are superposed on the type II burst lanes and the type II burst heights agree with the CME heights, suggesting that a CME bow shock propagates through variable plasma structures that cause the radio enhancements. In category 2 events, the type II burst heights agree with the CME leading front heights and the radio enhancements appear when the CME approaches an earlier-launched CME, suggesting CME–CME interaction to be the cause. In category 3 events, the type II heights are

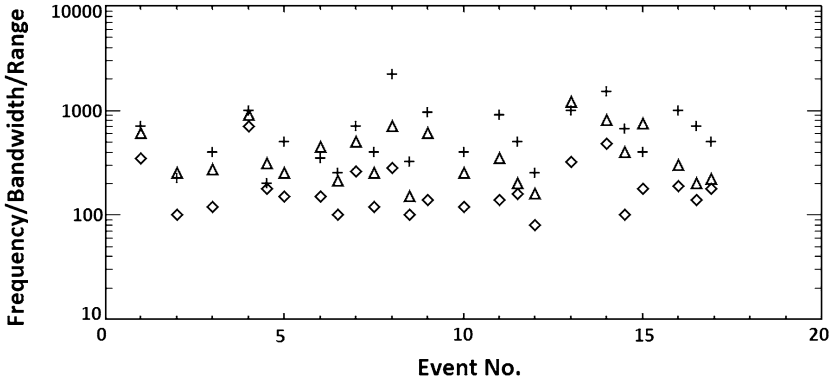

Figure 18 Characteristics of each radio enhancement. The plotted values are the frequency at the start of the enhancement (*cross*), the average bandwidth during the enhancement (*diamond*), and the maximum instantaneous range of emission (*triangle*), all expressed in kHz.

lower than the CME heights almost from the start, indicating a shock at the CME flanks, and interaction with a close-by streamer apparently is the cause for the radio enhancement. In category 4 events, the radio enhancements are located within wide-band type II burst emission, with unknown characteristics and origin. In category 5 events, the radio enhancements are associated with type III bursts (fast particle beams) that stop near the type II burst frequency. The categories are described in more detail in Section 4.

The smallest variation in start frequencies (Figure 18) and average bandwidths was in category 4 (enhancements located within wide-band type II burst emission), indicating that the enhancements had similar start frequencies and bandwidths. These were also long-duration enhancements, lasting for two to three hours, except for one that lasted only for 14 minutes. In general, the radio enhancements showed a variety of durations, ranging from seven minutes to almost four hours. In category 1 (enhancements superposed on a type II burst lane), there were no long-duration enhancements as they all had a duration of one hour or less.

In two events the frequency drift of the radio emission was clearly faster than in the other events. In both cases, the start frequency was high and the enhanced emission followed the type II lane, so the observed frequency drift of the enhancement corresponded to the type II shock speed. Of these two, event 13 was classified as a category 2 (CME–CME interaction) event and event 14 as a category 1 event.

All three enhancements that showed a low-frequency extension in their emission were classified as category 3 events (CME flank–streamer interaction). In category 5 (events associated with type III bursts), there was only one clear case and two possible associations.

Cross-correlating the characteristics did not reveal any clear associations with particular category types. In general, the bandwidth of the emission decreased as the start frequency decreased, reflecting the decreasing density in the solar corona.

3. Discussion

Different scenarios on how the enhanced radio signatures can be created were discussed in this article. The CME–CME interaction may produce radio enhancements if the CMEs propagate from the same or a nearby active region and the later-launched CME catches up with the earlier one (Gopalswamy *et al.*, 2001b). As high-speed CMEs often show bow

shocks or driven shocks, there is also the possibility of shock–CME interaction and shock–shock interaction (Lugaz, Manchester, and Gombosi, 2005; Lugaz *et al.*, 2008, 2009). There can also be interaction at the flanks of the CMEs, not only at the leading fronts (Holman and Pesses, 1983). Interaction may also occur between a CME and a streamer (Cho *et al.*, 2008, 2011).

Interaction as a physical process can also occur in different ways. Two CMEs can merge into one, which is usually observed as a change in the CME velocity (Gopalswamy *et al.*, 2001a; Burlaga, Plunkett, and St. Cyr, 2002). A CME may also meet the material of an earlier CME, however, and continue to propagate at the same speed. Alternatively, the velocity of the earlier CME can increase and the primary CME velocity decrease after the interaction (Maričić *et al.*, 2014).

As type II emission is due to accelerated electrons at the propagating shock front, an enhancement implies that more electrons are accelerated. The obvious source would be the material of another CME, or irregularities in the solar wind. Fast-propagating particle beams that originate from later flares could also bring more particles to the shock front, see for example Figure 3 of Reiner *et al.* (2008), and cause enhanced radio emission. One of our radio enhancement events (event 12) appears to have such a possibility. The type III bursts were observed during the type II burst enhancement, but the type IIIs did not continue below the type II burst frequencies. This implies that the particle beams could not get past the shock. The type III activity during another event (event 1) suggests that this radio enhancement may not have been a sign of a CME interaction alone, but a combination of both processes.

There are various sources of error when CME and radio burst heights are compared. The chosen atmospheric density model may not represent the true coronal conditions, and therefore the type II burst source heights may not be correct. Misinterpreting harmonic emission as fundamental emission will also cause an error in the source height estimation. Finally, if the emission lane is wide, the decision which part of the lane to use for calculations will have an effect on the heights. The CME heights also contain errors, especially in the case of halo-type CMEs that propagate towards the observer. The observer sees a projection of the true CME, and the observed speed may be partly propagation velocity and partly expansion velocity.

In order to estimate the uncertainties in measured CME heights and to evaluate their possible effects on event classification, we compared our values with measurements presented in several publications.

For event 1, our measurements of CME2 heights from STEREO A agree well with the height–time measurements of Maričić *et al.* (2014) up to $\sim$13 $R_\odot$, where our measurements end. SOHO/LASCO heights, however, are significantly lower, probably because of projection effects. For CME1 we only present extrapolated values from LASCO in Figure 1, and they are significantly lower than those of Maričić *et al.* (2014) from STEREO A and B. For event 1, Temmer *et al.* (2014) also reported heights of both CME1 and CME2 measured at different position angles. Their CME2 heights at position angle 100° start from above our last data point (from $\sim$ 15.6 $R_\odot$), but they agree reasonably well with our measurements. For CME1, the heights observed by LASCO are again significantly lower than those of Temmer *et al.* (2014) from STEREO.

For events 2 and 6, we compared our CME heights with those of Xie *et al.* (2013), who used measurements from the *Heiospheric Imager* on STEREO. In event 2, our measurements of CME2 heights from STEREO A can be smoothly extrapolated to their measurements, while the LASCO heights rise somewhat more rapidly and are 3 – 4 $R_\odot$ above theirs in the overlapping time range. In event 6, our LASCO and STEREO A heights of CME2 are in satisfactory agreement with those of Xie *et al.* (2013).

Event 7 has been extensively studied by Magdalenić *et al.* (2014), who derived the radio source heights by triangulation. Again, our CME2 height measurements from STEREO B agree well with those of Magdalenić *et al.* (2014). Magdalenić *et al.* (2014) also used STEREO B *Heliospheric Imager* data to determine the CME2 front heights. These agree well with our STEREO COR measurements, but already from below 10 $R_\odot$, they deviate significantly from our LASCO heights, which are higher. LASCO heights continue up to 26.4 $R_\odot$, where they match the lowest radio source height derived by triangulation quite well.

Our measurements of CME2 heights from LASCO are in good agreement with Ding *et al.* (2014) for event 13. At low heights, our results from STEREO B also agree, although already from about 8 $R_\odot$, STEREO B results are systematically somewhat higher than those from LASCO, but still with only relatively small 1 – 1.5 $R_\odot$ differences.

For event 15, we were only able to compare the CME height with those of Möstl *et al.* (2015). From their Figure 2 we obtained values that are in reasonable agreement with our LASCO measurements below 7 $R_\odot$, and an extrapolation of the last LASCO heights from $\sim$23 to 26 $R_\odot$ continues smoothly to the heights derived by Möstl *et al.* (2015).

Radio direction finding, also known as triangulation measurements, is a useful method to locate the radio source positions when observations are available from two or more spacecraft, see, *e.g.* Reiner *et al.* (2009). Most often, this method has been applied to type III bursts, but recently, several IP type II bursts have been analysed, to determine their locations. Our sample includes two of them, events 7 and 13.

For event 7, Magdalenić *et al.* (2014) determined that the radio source positions were located near the southern flank of the CME, but the source heights from radio triangulation were about 20 $R_\odot$ higher than what the standard coronal atmospheric density models would give for the flank. However, we note that the radio heights from triangulation are a direct continuation to the LASCO CME2 leading front heights, suggesting that the emission source (driver) was propagating in an unexpectedly dense plasma region. For event 13, the radio source locations at 800 – 1000 kHz were found to be near the CME leading front (Mäkelä *et al.*, 2016). However, at frequencies lower than 800 kHz, triangulation gave unrealistically large height values.

Similar large radio source heights were obtained recently by Krupar *et al.* (2016) when analysing the CME event on 29 November 2013. The heights from radio triangulation were 26 – 66 $R_\odot$, while calculated from the atmospheric density model, the heights were only 6.5 – 21.5 $R_\odot$. The modelled CME leading front heights were in between those values. In this case, the radio source directions also suggested that the emission was created near the flanks of the CME.

As direction finding looks to be sensitive to radio propagation effects in the IP medium and the radio sources could even be spatially extended at large distances, more studies on type II burst locations are clearly needed.

4. Summary and Conclusions

In this study we have analysed IP type II bursts that show enhancements in their radio emission. The studied sample consists of 16 events from the time period of 2011 – 2014. The selected period allowed us to obtain a 3D view of the events, with the good data coverage from SOHO, *Wind*, and the two STEREO spacecraft on opposite sides of the Sun. One idea was to verify whether CME interaction can cause the radio enhancements.

Based on our analysis, we found that the radio enhancements can be divided into five different categories depending on their origin.

1) Events where the type II heights agree with the CME heights, indicating that the shock is located at the leading front of the CME. The radio enhancements are superposed on the type II lanes and are probably due to irregularities in the solar wind, *i.e.* the shock meets remnant material from earlier CMEs, but continues to propagate at the same speed. *Events 1, 8–first part, and 14. Earlier triangulation results also suggest that event 7 could belong to this category.*

2) Events where the type II heights agree with the CME leading front heights, within the estimated error margins. The radio enhancements appear at a time when the later CME reaches heights that are $1.5 - 7.5\ R_{\odot}$ lower than the heights of the earlier CME, or soon after reaching the same heights. This suggests interaction/merging of the CMEs. In some of these cases, frequency/density jumps are observed in the radio spectra. *Events 4–first part, 5, 13, and 16.*

3) Events where the type II heights are significantly lower than the CME heights almost from the start, and the separation in height grows in time. It is possible that in these cases the shock is located somewhere below the CME leading front. From the LASCO and SECCHI images it can be seen that in most of these cases, the earlier CMEs did not seem to be at sufficiently low height or dense enough to be causing excess densities. In some cases, CME merging, if any, would have already occurred when the radio enhancements appeared. In all of these cases, there were streamers within the direction of the CME/shock propagation, suggesting that CME flank–streamer interaction could have been the cause for the enhanced radio emission. Event 10 appears to have both a CME bow shock and a shock at the flanks, but the enhancement appears to be due to a flank shock–streamer interaction. *Events 2, 3, 4–later part, 7, 9, 10, and 11.*

4) Events where the radio enhancements are located within wide-band type II burst emission. Wide-band events have been analysed earlier (Pohjolainen, Allawi, and Valtonen, 2013), and they may have a different origin compared to the 'regular' type II bursts. *Events 6, 8–later part, and 15.*

5) Events where the radio enhancements occur when later-accelerated particles, observed as type III bursts, stop near the type II burst frequency. Enhanced emission could be created when the particle beams meet the CME or shock front and become trapped in the magnetic field. Alternatively, the enhanced emission could be due to observing the two different emissions on top of each other. Type III burst cut-off, *i.e.* type III emission lanes ending at type II burst frequencies, have been reported earlier by Pohjolainen, Al-Hamadani, and Valtonen (2016), but in these cases, there were no obvious enhancements in the type II emission bands. *Event 12, possibly also events 1 and 9.*

The drift rates or the bandwidth characteristics or cross-correlations of various characteristics did not reveal any clear association with particular category types. Our conclusion is that the enhanced radio emission, observed during IP type II bursts and associated with CMEs and propagating shocks, can have different origins. We found that CME–CME interaction is the most probable cause in 25% of the events, but in most cases (38%), CME flank–streamer interaction looks more probable. The type II emission may also originate either from a CME bow shock or a CME flank shock, which affects the configuration in relation to streamers. Some more unusual events were also found (wide-band enhancements, type III-burst related enhancements), but these remain less clear because of the small number of events.

Acknowledgements This work was supported by grant 4438/2013 from the Ministry of Higher Education and Scientific Research of Iraq. We are grateful to all the individuals who have contributed by creating and

updating the various solar event catalogues. The CME Catalog is generated and maintained at the CDAW Data Center by NASA and the Catholic University of America in cooperation with the Naval Research Laboratory. The *Wind* WAVES radio type II burst catalogue has been prepared by Michael L. Kaiser and is maintained at the Goddard Space Flight Center. SOHO is a project of international cooperation between ESA and NASA.

Disclosure of Potential Conflicts of Interest The authors declare that they have no conflicts of interest.

References

Bale, S.D., Reiner, M.J., Bougeret, J.-L., Kaiser, M.L., Krucker, S., Larson, D.E., Lin, R.P.: 1999, *Geophys. Res. Lett.* **26**, 1573. DOI.

Bemporad, A., Mancuso, S.: 2010, *Astrophys. J.* **720**, 130. DOI.

Bougeret, J.-L., Kaiser, M.L., Kellogg, P.J., Manning, R., Goetz, K., Monson, S.J., Monge, N., Friel, L., Meetre, C.A., Perche, C., Sitruk, L., Hoang, S.: 1995, *Space Sci. Rev.* **71**, 231. DOI.

Bougeret, J.-L., Goetz, K., Kaiser, M.L., Bale, S.D., Kellogg, P.J., Maksimovic, M., *et al.*: 2008, *Space Sci. Rev.* **136**, 487. DOI.

Brueckner, G.E., Howard, R.A., Koomen, M.J., Korendyke, C.M., Michels, D.J., Moses, J.D., Socker, D.G., Dere, K.P., Lamy, P.L., Llebaria, A., Bout, M.V., Schwenn, R., Simnett, G.M., Bedford, D.K., Eyles, C.J.: 1995, *Solar Phys.* **162**, 357. DOI.

Burlaga, L.F., Plunkett, S.P., St. Cyr, O.C.: 2002, *J. Geophys. Res.* **107**, 1266. DOI.

Cairns, I.-H., Knock, S.-A., Robinson, P.-A., Kuncic, Z.: 2003, *Space Sci. Rev. Astrophys.* **107**, 827. DOI.

Cane, H.V., Sheeley, N.R. Jr., Howard, R.A.: 1987, *J. Geophys. Res.* **92**, 9869. DOI.

Cho, K.-S., Bong, S.-C., Kim, Y.-H., Moon, Y.-J., Dryer, M., Shanmugaraju, A., Lee, J., Park, Y.D.: 2008, *Astron. Astrophys.* **491**, 873. DOI.

Cho, K.-S., Bong, S.-C., Moon, Y.-J., Shanmugaraju, A., Kwon, R.-Y., Park, Y.D.: 2011, *Astron. Astrophys.* **530**, A16. DOI.

Delaboudinière, J.-P., Artzner, G.E., Brunaud, J., Gabriel, A.H., Hochedez, J.F., Millier, F., *et al.*: 2014, *Solar Phys.* **162**, 291. DOI.

Ding, L-G., Li, G., Jiang, Y., Le, G-M., Shen, C-L., Wang, Y-M., Chen, Y., Xu, F., Gu, B., Zhang, Y-N.: 2014, *Astrophys. J.* **793**, L35. DOI.

Gopalswamy, N., Yashiro, S., Kaiser, M.L., Howard, R.A., Bougeret, J.-L.: 2001a, *Geophys. Res. Lett.* **106**, 29219. DOI.

Gopalswamy, N., Yashiro, S., Kaiser, M.L., Howard, R.A., Bougeret, J.L.: 2001b, *Astrophys. J. Lett.* **548**, L91. DOI.

Gopalswamy, N., Yashiro, S., Kaiser, M.L., Howard, R.A., Bougeret, J.-L.: 2002, *Geophys. Res. Lett.* **29**, 106. DOI.

Gopalswamy, N., Mäkelä, P., Yashiro, S., Xie, H., Akiyama, S., Thakur, N.: 2015, *J. Phys. Conf. Ser.* **642**, 012012. DOI.

Holman, G.D., Pesses, M.E.: 1983, *Astrophys. J.* **276**, 837. DOI.

Howard, R.A., Moses, J.D., Vourlidas, A., Newmark, J.S., Socker, D.G., Plunkett, S.P., *et al.*: 2008, *Space Sci. Rev.* **136**, 67. DOI.

Kai, K., Melrose, D.B., Suzuki, S.: 1985, In: McLean, D.J., Labrum, N.R. (eds.) *Solar Radiophysics*, Cambridge University Press, New York.

Krupar, V., Eastwood, J.P., Kruparova, O., Santolik, O., Soucek, J., Magdalenic, J., Vourlidas, A., Maksimovic, M., Bonnin, X., Bothmer, V., Mrotzek, N., Pluta, A., Barnes, D., Davies, J.A., Martínez Oliveros, J.C., Bale, S.D.: 2016, *Astrophys. J. Lett.* **823**, L5. DOI.

Leblanc, Y., Dulk, G.A., Bougeret, J.-L.: 1998, *Solar Phys.* **183**, 165. DOI.

Lin, R.P., Potter, D.W., Gurnett, D.A., Scarf, F.L.: 1981, *Astrophys. J.* **251**, 364. DOI.

Liu, Y.D., Luhmann, J.G., Lugaz, N., Möstl, C., Davies, J.A., Bale, S.D., Lin, R.P.: 2013, *Astrophys. J.* **769**, 45. DOI.

Lugaz, N., Manchester, W.B. IV, Gombosi, T.I.: 2005, *Astrophys. J.* **634**, 651. DOI.

Lugaz, N., Manchester, W.B. IV, Roussev, I.I., Gombosi, T.I.: 2008, *J. Atmos. Solar-Terr. Phys.* **70**, 598. DOI.

Lugaz, N., Vourlidas, A., Roussev, I.I., Morgan, H.: 2009, *Solar Phys.* **256**, 269. DOI.

Magdalenić, J., Marqué, C., Krupar, V., Mierla, M., Zhukov, A.N., Rodriguez, L., Maksimović, M., Cecconi, B.: 2014, *Astrophys. J.* **791**, 115. DOI.

Mäkelä, P., Gopalswamy, N., Reiner, M.J., Akiyama, S., Krupar, V.: 2016, *Astrophys. J.* **827**, 141. DOI.

Maričić, D., Vršnak, B., Dumbović, M., Žic, T., Roša, D., Hržina, D., Lulić, S., Romštajn, I., Bušić, I., Salamon, K., Temmer, M., Rollett, T., Veronig, A., Bostanjyan, N., Chilingarian, A., Mailyan, B., Arakelyan, K., Hovhannisyan, A., Mujić, N.: 2014, *Solar Phys.* **289**, 351. DOI.

Martínez Oliveros, J.C., Raftery, C.L., Bain, H.M., Liu, Y., Krupar, V., Bale, S., Krucker, S.: 2012, *Astrophys. J.* **748**, 66. DOI.
Mays, M.L., Thompson, B.J., Jian, L.K., Colaninno, R.C., Odstrcil, D., Möstl, C., Temmer, M., Savani, N.P., Collinson, G., Taktakishvili, A., MacNeice, P.J., Zheng, Y.: 2015, *Astrophys. J.* **812**, 145. DOI.
Möstl, C., Amla, K., Hall, J.R., Liewer, P.C., De Jong, E.M., Colaninno, R.C., Veronig, A.M., Rollett, T., Temmer, M., Peinhart, V., Davies, J.A., Lugaz, N., Liu, Y.D., Farrugia, C.J., Luhmann, J.G., Vršnak, B., Harrison, R.A., Galvin, A.B.: 2014, *Astrophys. J.* **787**, 119. DOI.
Möstl, C., Rollett, T., Frahm, R.A., Liu, Y.D., Long, D.M., Colaninno, R.C., Reiss, M.A., Temmer, M., Farrugia, C.J., Posner, A., Dumbović, M., Janvier, M., Démoulin, P., Boakes, P., Devos, A., Kraaikamp, E., Mays, M.L., Vršnak, B.: 2015, *Nat. Commun.* **6**, 7135. DOI.
Newkirk, G. Jr.: 1961, *Astrophys. J.* **133**, 983. DOI.
Odstrcil, D., Vandas, M., Pizzo, V.J., MacNeice, P.: 2003, In: Velli, M., Bruno, R., Malara, F., Bucci, B. (eds.) *Tenth International Solar Wind Conf.*, *AIP Conf. Proc.* **679**, 699. DOI.
Papaioannou, A., Souvatzoglou, G., Paschalis, P., Gerontidou, M., Mavromichalaki, H.: 2014, *Solar Phys.* **289**, 423. DOI.
Pohjolainen, S., Al-Hamadani, F., Valtonen, E.: 2016, *Solar Phys.* **291**, 487. DOI.
Pohjolainen, S., Allawi, H., Valtonen, E.: 2013, *Astron. Astrophys.* **558**, A7. DOI.
Pohjolainen, S., van Driel-Gesztelyi, L., Culhane, J.L., Manoharan, P.K., Elliott, H.A.: 2007, *Solar Phys.* **244**, 167. DOI.
Reiner, M.J., Karlický, M., Jiřička, K., Aurass, H., Mann, G., Kaiser, M.L.: 2000, *Astrophys. J.* **530**, 1049. DOI.
Reiner, M.J., Klein, K.-L., Karlicky, M., Jiricka, K., Klassen, A., Kaiser, M.L., Bougeret, J.-L.: 2008, *Solar Phys.* **249**, 337. DOI.
Reiner, M.J., Goetz, K., Fainberg, J., Kaiser, M.L., Maksimovic, M., Cecconi, B., Hoang, S., Bale, S.D., Bougeret, J.-L.: 2009, *Solar Phys.* **259**, 255. DOI.
Saito, K.: 1970, *Ann. Tokyo Astron. Obs.* **12**, 53.
Shanmugaraju, A., Prasanna Subramanian, S., Vrsnak, B., Ibrahim, M.S.: 2014, *Solar Phys.* **289**, 4621. DOI.
Teklu, T.B., Gholap, A.V., Gopalswamy, N., Yashiro, S., Mäkelä, P., Akiyama, S., Thakur, N., Xie, H.: 2016, URSI Asia-Pacific Radio Science Conference, Seoul, 2016, *ArXiv e-prints* arXiv.
Temmer, M., Vršnak, B., Rollett, T., Bein, B., de Koning, C.A., Liu, Y., Bosman, E.: 2012, *Astrophys. J.* **749**, 57. DOI.
Temmer, M., Veronig, A.M., Peinhart, V., Vršnak, B.: 2014, *Astrophys. J.* **785**, 85. DOI.
Vandas, M., Fischer, S., Dryer, M., Smith, Z., Detman, T., Geranios, A.: 1997, *Geophys. Res. Lett.* **102**, 22295. DOI.
Vršnak, B., Magdalenič, J., Zlobec, P.: 2004, *Astron. Astrophys.* **413**, 753. DOI.
Wu, S.T., Wang, A.H., Gopalswamy, N.: 2002, In: Sawaya-Lacoste, H. (ed.) *SOLMAG 2002*, *ESA SP-505*, 227.
Wu, C-C., Liou, K., Vourlidas, A., Plunkett, S., Dryer, M., Wu, S.T., Mewaldt, R.A.: 2016, *J. Geophys. Res.* **121**, 56. DOI.
Wuelser, J.-P., Lemen, J.R., Tarbell, T.D., Wolfson, C.J., Cannon, J.C., Carpenter, B.A., *et al.*: 2004, EUVI: the STEREO-SECCHI extreme ultraviolet imager. In: Fineschi, S., Gummin, M.A. (eds.) *Telescopes and Instrumentation for Solar Astrophysics*, *Soc. Photo-Optical Instrum. Eng. (SPIE)*, 111. DOI.
Xie, H., St. Cyr, O.C., Gopalswamy, N., Odstrcil, D., Cremades, H.: 2013, *J. Geophys. Res.* **118**, 4711. DOI.
Zucca, P., Carley, E.P., Bloomfield, D.S., Gallagher, P.T.: 2014, *Astron. Astrophys.* **564**, A47. DOI.